Kinetic energy transfers between mesoscale and submesoscale motions in the open ocean's upper layers

Alberto C. Naveira Garabato*

Ocean and Earth Science, University of Southampton, Southampton, U.K.

Xiaolong Yu†

Laboratoire d'Océanographie Physique et Spatiale, Ifremer, Université de Bretagne Occidentale, Brest, France

School of Marine Sciences, Sun Yat-sen University, Zhuhai, China

Jörn Callies

California Institute of Technology, Pasadena, California

Roy Barkan

Department of Atmospheric and Oceanic Sciences, University of California, Los Angeles, Los Angeles, California

Department of Geosciences, Tel Aviv University, Ramat Aviv, Israel

Kurt L. Polzin

Woods Hole Oceanographic Institution, Woods Hole, Massachusetts

Eleanor E. Frajka-Williams

National Oceanography Centre, Southampton, U.K.

Christian E. Buckingham

Laboratoire d'Océanographie Physique et Spatiale, Ifremer, Université de Bretagne Occidentale, Brest, France

British Antarctic Survey, Cambridge, U.K.

Stephen M. Griffies

NOAA Geophysical Fluid Dynamics Laboratory, and Program in Atmospheric and Oceanic Sciences, Princeton University, Princeton, New Jersey

[*] *Corresponding author*: Alberto C. Naveira Garabato, acng@noc.soton.ac.uk

[†] *Corresponding author*: Xiaolong Yu, xiaolong.yu@ifremer.fr

ABSTRACT

Mesoscale eddies contain the bulk of the ocean's kinetic energy (KE), but fundamental questions remain on the cross-scale KE transfers linking eddy generation and dissipation. The role of submesoscale flows represents the key point of discussion, with contrasting views of submesoscales as either a source or a sink of mesoscale KE. Here, the first observational assessment of the annual cycle of the KE transfer between mesoscale and submesoscale motions is performed in the upper layers of a typical open-ocean region. Although these diagnostics have marginal statistical significance and should be regarded cautiously, they are physically plausible and can provide a valuable benchmark for model evaluation. The cross-scale KE transfer exhibits two distinct stages, whereby submesoscales energize mesoscales in winter and drain mesoscales in spring. Despite this seasonal reversal, an inverse KE cascade operates throughout the year across much of the mesoscale range. Our results are not incompatible with recent modeling investigations that place the headwaters of the inverse KE cascade at the submesoscale, and that rationalize the seasonality of mesoscale KE as an inverse cascade-mediated response to the generation of submesoscales in winter. However, our findings may challenge those investigations by suggesting that, in spring, a downscale KE transfer could dampen the inverse KE cascade. An exploratory appraisal of the dynamics governing mesoscale-submesoscale KE exchanges suggests that the upscale KE transfer in winter is underpinned by mixed-layer baroclinic instabilities, and that the downscale KE transfer in spring is associated with frontogenesis. Current submesoscale-permitting ocean models may substantially understate this downscale KE transfer, due to the models' muted representation of frontogenesis.

1. Introduction

Mesoscale eddies – geostrophically near-balanced flows with characteristic horizontal scales of tens to a few hundred kilometres and time scales of weeks to months – are ubiquitous in the ocean, and play a fundamental role in the global circulation. As well as accounting for almost 80% of the total oceanic kinetic energy (KE) (Ferrari and Wunsch, 2009; Chelton et al., 2011; Morrow and Le Traon, 2012), mesoscale eddies effect substantial (horizontal and vertical) transports of momentum, heat, freshwater, carbon and nutrients, thereby shaping the time-mean oceanic flow field and property distributions in a range of climatically important ways (e.g., Hallberg and Gnanadesikan, 2006; Griffies et al., 2015; Llort et al., 2018; Busecke and Abernathey, 2019; Sun et al., 2019). Determining the lifecycle of mesoscale eddies and, specifically, the pathways of KE between eddy generation and dissipation, is thus essential to understand the dynamical controls on the ocean circulation and its climatic role. However, considerable uncertainties persist around both the generation and dissipation of mesoscale eddies, linked to divergent views on the direction of, and mechanisms underpinning, the transfer of KE between oceanic flows of different scales.

The classical paradigm of the mesoscale eddy lifecycle is founded on geostrophic turbulence theory (Gill et el., 1974; Rhines, 1975, 1979; Salmon, 1978, 1980; Smith and Vallis, 2002; Ferrari and Wunsch, 2009). In this view, mesoscale eddy generation stems from (i) the input of potential energy to the ocean via the action of wind and surface buoyancy fluxes at the large horizontal scales of basins, and (ii) the conversion of that potential energy to KE by baroclinic instability of the ocean's major current systems, at horizontal scales close to the first baroclinic Rossby radius (typically on the order of tens of kilometres; Chelton et al., 1998). An inverse KE cascade ensues, in which nonlinear eddy-eddy interactions transfer KE toward larger scales. The inverse KE cascade ultimately ceases at scales for which Rossby wave dispersion becomes significant,

leading to the emergence of zonal jets (Rhines, 1975; Panetta, 1993). Dissipation of mesoscale eddies is posited to occur through frictional processes at the top and bottom boundaries, favoured by the KE transfer toward ever-growing vertical scales implicit in the inverse cascade. Substantial evidence in support of this paradigm is found in satellite altimetric observations (Scott and Wang, 2005; Tulloch et al., 2011) and mesoscale-resolving ocean models (Arbic et al., 2013, 2014), both of which reveal an inverse KE cascade across horizontal scales typical of mesoscale eddies. These observations and models also indicate the occurrence of a notable seasonal cycle in mesoscale KE, whereby generalised increases in KE in spring (for mid-gyre environments) or summer (for western boundary currents) are often interpreted in terms of processes consistent with the classical eddy lifecycle paradigm (Scharffenberg and Stammer, 2010; Qiu et al., 2014; Rieck et al., 2015; Zhai, 2017) and atmospheric damping of mesoscale KE (Zhai et al., 2008; Rai et al., 2021).

In recent years, rapid advances in theoretical understanding of submesoscale dynamics in the ocean surface boundary layer (see e.g., McWilliams (2016) for a review) have begun to challenge some important aspects of the above view. Submesoscale flows are, like mesoscale motions, in partial geostrophic balance, but are characterized by smaller horizontal scales (typically on the order of a kilometre), shorter time scales (on the order of an inertial period), higher Rossby numbers, and lower KE levels than mesoscale flows. Submesoscale motions are commonly generated as wind and surface buoyancy fluxes – the very same forcings that supply potential energy to the ocean in the classical eddy lifecycle paradigm – act on the lateral density fronts that populate the ocean's upper layers (Thomas, 2005; Thomas and Ferrari, 2008; Taylor and Ferrari, 2010; D'Asaro et al., 2011; Brannigan et al., 2017; Yu et al., 2019a). This has motivated the proposition, now supported by submesoscale-permitting ocean models (Sasaki et al., 2014, 2017; Uchida et al., 2017; Dong et al., 2020; Schubert et al., 2020), that substantial conversion of potential energy to mesoscale KE occurs not via baroclinic instability of major currents, but through an inverse

cascade of submesoscale KE initiated by upper-ocean frontal instabilities (Klein et al., 2019). A role of submesoscale motions as the headwaters of the inverse KE cascade appears at odds with their well-documented association with intense turbulent dissipation (D'Asaro et al., 2011; Yu et al., 2019a), which instead points to the existence of a direct KE cascade at the submesoscale mediated by loss of balance and the generation of divergent, ageostrophic motions (Capet et al., 2008a,b; Molemaker and McWilliams, 2010; Molemaker et al., 2010; Barkan et al., 2015; Poje et al., 2017). However, a submesoscale-triggered inverse KE cascade is often invoked to explain the seasonal cycle of mesoscale KE in submesoscale-permitting models (Qiu et al., 2014; Sasaki et al., 2014; Uchida et al., 2017; Dong et al., 2020; Schubert et al., 2020), in which the spring / summer increase in mesoscale KE is a delayed, inverse cascade-mediated response to the generation of submesoscale KE by strong atmospheric forcing of upper-ocean fronts in winter. A wintertime intensification of submesoscale KE has been corroborated by observations (Callies et al., 2015; Buckingham et al., 2016, 2019).

In summary, there are conflicting views on the direction and controlling processes of the cross-scale KE transfers linking mesoscale eddy generation and dissipation – with the role of submesoscales representing the key point of discussion. A critical obstacle to the resolution of this problem has been the unavailability to date of observations featuring both the high spatio-temporal resolution (resolving the small horizontal scales and short time scales of submesoscales) and extent (capturing many (sub-)mesoscale eddy events) required to characterize KE transfers between submesoscale and mesoscale motions. Such observations are essential to assess the reliability of KE cascade diagnostics based on global or regional ocean models that at best permit, rather than fully resolve, submesoscale flows. Here, we address this issue by evaluating the annual cycle of the cross-scale KE transfer in a typical mid-gyre region, using a unique data set that meets the calculation's required resolution and extent criteria. The theory of cross-scale KE transfers, data set and

analysis methodology are outlined in section 2. Results are presented in section 3, and discussed in section 4. Our diagnostics have marginal statistical significance and should thus be regarded cautiously. However, they are also physically plausible, and can provide a valuable benchmark against which to evaluate model-based perspectives on the cross-scale KE transfer problem.

Our main finding is that the KE transfer between submesoscale and mesoscale motions exhibits two distinct seasonal stages, with an upscale KE transfer in winter (defined as December to February in this work) and a downscale KE transfer in spring (defined as March to May) suggestively associated with distinct upper-ocean dynamics. We show that only the upscale KE transfer stage is successfully reproduced by a state-of-the-art, submesoscale-permitting ocean model, likely as a result of the model's sub-optimal representation of the frontogenetic processes underpinning the downscale KE transfer. The implications of our results for the ongoing debate on the lifecycle of mesoscale eddies are considered in section 5, where conclusions are offered.

2. Theory, data and methodology

a. Theoretical framework of cross-scale KE transfers

Our definition of the cross-scale horizontal KE transfer (i.e. the transfer of horizontal KE between flows of different scales) is founded on the 'coarse-graining' framework, which was introduced to physical oceanography only recently (Aluie et al., 2018) but is well established in other fields (Leonard, 1974; Germano, 1992; Eyink, 2005). The technique permits the direct quantification of the nonlinear coupling between different flow scales, and provides a measure of the rate and direction (upscale or downscale) of KE being transferred between different scales at every spatial and / or temporal point in a given data set. A strength of the coarse-graining approach is its

generality, as it is free of the assumptions of homogeneity or isotropy implicit in other frameworks (e.g., Frisch, 1995).

The coarse-graining method entails the filtering of the horizontal velocity field $\mathbf{u_h}(\mathbf{x},t)$ (where $\mathbf{u_h} = (u,v)$, $\mathbf{x} = (x,y)$ is the spatial position vector, and t is time) with complementary low-pass and high-pass filters, in order to partition the scales in the system into larger ($\overline{\mathbf{u_h}}_l(\mathbf{x},t)$) and smaller ($\mathbf{u_h}(\mathbf{x},t) - \overline{\mathbf{u_h}}_l(\mathbf{x},t)$) than a specified spatial or temporal scale l (Aluie et al., 2018). This simple decomposition preserves the fundamental physical properties of the flow and, when applied to the dynamical equations, yields an expression for the horizontal KE transfer across scale l, $\Pi_l(\mathbf{x},t)$, such as

$$\Pi_l(\mathbf{x},t) = -\frac{1}{2}(\nabla_\mathbf{h}\overline{\mathbf{u_h}}_l + \nabla_\mathbf{h}\overline{\mathbf{u_h}}_l^T) : (\overline{\mathbf{u_h}\mathbf{u_h}}_l - \overline{\mathbf{u_h}}_l\overline{\mathbf{u_h}}_l), \tag{1}$$

where ∇_h and ^{T} respectively denote the horizontal gradient and transpose operators, the colon : is a tensor inner product that generates a scalar, and positive (negative) values of Π_l indicate horizontal KE transfers directed toward larger (smaller) values of l. See Aluie et al. (2018) for details of this derivation. As noted by these authors, the coarse-graining approach is superior to other methods in that it satisfies Galilean invariance, while other approaches are affected by a gauge freedom and so do not provide a unique definition of the cross-scale horizontal KE transfer.

In this work, we use (1) to quantify the KE transfer between submesoscale and mesoscale motions, by differentiating between the two classes of flow in terms of their frequency, ω (i.e. l is taken as ω in our application of (1); see section 2c). Thus, we hereafter refer to the cross-scale KE transfer as Π_ω. Note that, from a mathematical perspective, the coarse-graining approach can be indistinctively applied in the wavenumber and frequency domains. A discussion and explicit demonstration of this statement is provided by Barkan et al. (2017). The coarse-graining method draws parallels with an extensive literature focussed on the representation of sub-grid-scale turbulent processes in ocean models, in which relationships between such processes and the properties of coarser flows

are assessed and utilised for the development of parameterizations (e.g., Gent et al., 1995; Griffies, 1998; McDougall and McIntosh, 2001; Eden and Greatbatch, 2008; Marshall et al., 2012).

b. Data

Our analysis makes use of two data sets, described in sequence below. The primary data set comprises a suite of observations of the evolution of upper-ocean hydrography and horizontal velocity over one annual cycle in a typical mid-gyre area. The second data set consists of the output of a submesoscale-permitting global ocean model.

1) Observations

The measurements analyzed here were obtained by nine bottom-anchored subsurface moorings deployed over the Porcupine Abyssal Plain site in the northeast Atlantic Ocean for the period September 2012 - September 2013 (Fig. 1a), under the auspices of the OSMOSIS (Ocean Surface Mixing - Ocean Submesoscale Interaction Study) project (Buckingham et al., 2016; Damerell et al., 2016; Thompson et al., 2016). The site is in an abyssal plain of depth close to 4800 m. It is analogous to many open-ocean areas far away from the western boundaries of ocean basins and from complex topography, in that it hosts a weak time-mean circulation and moderate (sub-)mesoscale eddy and internal wave energy levels (Buckingham et al., 2016, 2019; Thompson et al., 2016; Yu et al., 2019b; Erickson et al., 2020; Callies et al., 2020). As such, it is expected to be broadly representative of mid-gyre regions across the extratropical global ocean. This expectation is endorsed by the observed seasonal cycles of mixed layer depth and mesoscale KE, which are comparable in magnitude and phase to those of many other mid-gyre areas elsewhere (section 3a). A caveat of our study is that, while such comparability suggests that our diagnosed seasonal contrast between cross-scale KE transfers in winter and spring is likely to be of wider spatio-

temporal representativeness, corroborating this finding will require observations of other regions and years.

The mooring array is arranged in two concentric quadrilaterals with a centrally located single mooring. The outer and inner quadrilaterals have respective side lengths of 13 km and 2.5 km. Thus, they respectively resolve mesoscale flows with horizontal scales as small as the local first-baroclinic Rossby radius (15 - 32 km), and submesoscale flows with horizontal scales comparable to the local mixed-layer Rossby radius (1 - 4 km) (Yu et al., 2019b; Callies et al., 2020). Mooring sensors comprised a series of paired Nortek Aquadopp acoustic current meters (ACMs) and Seabird MicroCAT conductivity - temperature - depth (CTD) instruments with a vertical inter-pair spacing of 30 - 100 m, spanning the approximate depth interval of 30 - 530 m (Fig. 1b). The central mooring was the most heavily instrumented, with thirteen CTD / ACM pairs. The inner and outer moorings had seven and five such pairs, respectively. Mooring observations captured most of the pycnocline and ocean interior throughout the year, and most of the mixed layer between November and April. CTD / ACM pairs sampled at temporal intervals of 5 - 10 min, with measurement errors that are negligible for the purposes of this work (Appendix A). The mooring measurements were complemented by hydrographic observations acquired by two ocean gliders that navigated in a bow-tie pattern across the mooring array for the entire sampling period (Damerell et al., 2016; Thompson et al., 2016).

The type of spatial arrangement used in the OSMOSIS array is rare in mooring deployments, and makes this data set particularly well suited to quantifying the mesoscale lateral gradients of horizontal velocity required for the calculation of Π_ω using (1). We will set these localized mooring-based diagnostics in a wider spatio-temporal context by repeating the calculation of Π_ω using surface geostrophic velocity fields derived from the delayed-time gridded $0.25^\circ \times 0.25^\circ$

AVISO global altimetric product, which affords effective horizontal and temporal resolutions of O(100 km) and O(1 month) (Ballarotta et al., 2019).

2) Numerical model

The output of one of the most realistic high-resolution ocean models (the LLC4320 simulation; Menemenlis et al., 2008; Arbic et al., 2018; Su et al., 2018) available for the OSMOSIS area is considered here to assess the robustness of observational results, enrich their interpretation, and probe the limitations of submesoscale-permitting models in representing cross-scale KE transfers. The LLC4320 simulation was performed using the MITgcm on a global latitude - longitude - cap (LLC) grid for a period of 14 months (limited by computational power requirements) between 10 September 2011 and 15 November 2012. The model has a horizontal grid spacing of $1/48^\circ$ (equivalent to a distance of 1.5-2.3 km in the OSMOSIS region) and 90 vertical levels (with spacings ranging from 1 m near the ocean surface to 480 m near the bottom), and thereby resolves mesoscale eddies and part of the internal wavefield and permits submesoscale variability. Horizontal wavenumber spectra suggest that the effective horizontal resolution of LLC4320 is about 10 km (Yu et al., 2019b). The model time step was 25 s, and model variables were stored as snapshots at hourly intervals. The model was forced with a prescribed atmospheric state (including 6-hourly 10-m wind velocity, 2-m air temperature and humidity, downwelling long- and short-wave radiation, and atmospheric pressure load) from the ECMWF operational reanalysis, using bulk formulae to compute turbulent air-sea fluxes. The model also used the full luni-solar tidal potential to force ocean tides. See Menemenlis et al. (2008), Arbic et al. (2018) and Su et al. (2018) for further details of the LLC4320 simulation.

c. Analysis

Measurements of temperature, salinity, pressure and horizontal velocity recorded by all moorings are (i) averaged onto hourly intervals between 5 September 2012 and 5 September 2013, (ii) linearly interpolated onto surfaces of constant depth at 10-m intervals between depths of 50 m and 520 m, and (iii) linearly interpolated onto uniform 10-min intervals. Potential density (referenced to the ocean surface) and depth are calculated from temperature, salinity and pressure using the Gibbs Seawater Oceanographic Toolbox (McDougall and Barker, 2011). Differences between potential and neutral densities, associated with compressibility effects, are estimated to be negligible over the uppermost 520 m (Yu et al., 2019b).

Our approach in this work is to distinguish between mesoscale and submesoscale motions by time scale, rather than follow a traditional, horizontal scale-based definition. Although this approach appears at odds with the classical formulation of geostrophic turbulence theory in horizontal wavenumber space (Rhines, 1975, 1979; Salmon, 1978, 1980), it is optimally suited to the OSMOSIS data set, which is finely resolved in time (with an effective temporal resolution of < 30 min) but poorly resolved in horizontal space (with only a small set of resolved horizontal distances, corresponding to the separations between pairs of moorings; Callies et al., 2020). Relating our results to those of previous studies thus requires the assertion that cross-scale KE transfers in frequency space map directly onto horizontal wavenumber space.

This assertion is founded on two factors. First, frequency and horizontal wavenumber spectra of subinertial (i.e. with frequencies lower than the inertial frequency, f) KE in the ocean are characteristically red (Ferrari and Wunsch, 2009; see also Frankignoul and Hasselmann, 1977): KE increases quasi-monotonically with decreasing frequency and horizontal wavenumber, such that slowly-evolving eddies are systematically larger than rapidly-evolving eddies. This feature of

the ocean's eddy field may be readily illustrated with a 2-d (frequency - horizontal wavenumber) spectrum of KE in the LLC4320 simulation of the OSMOSIS area (Fig. 2a), which reproduces the expected relationship between eddy frequency and horizontal size, and shows that such relationship breaks down for near- and superinertial internal wave motions (e.g., near-inertial waves and internal tides are characterized by horizontal wavenumbers as small as those of the lowest-frequency subinertial eddies). The recent analysis of Callies et al. (2020) directly confirms the key features of this model-based KE spectrum with the OSMOSIS data. Second, investigation of the KE cascades in mesoscale-permitting or -resolving numerical models of varying degree of realism (Arbic et al., 2012, 2014; Sérazin et al., 2018; O'Rourke et al., 2018) suggests that the rate and direction of KE transfers in frequency space are generally in agreement with those in horizontal wavenumber space, such that the KE transfers may be assessed in either space. Thus, over a wide range of scales and conditions, KE is expected to transfer toward slowly-evolving eddies as it transfers toward large eddies, and toward rapidly-evolving eddies as it transfers toward small eddies. We have corroborated that this expectation holds in the OSMOSIS area in the LLC4320 simulation (Appendix B). Note that, although relatively infrequent in the geostrophic turbulence context, a frequency-space formulation of KE transfers is common in studies of the interactions between (sub-)mesoscale eddies and internal waves (Polzin, 2010; Barkan et al., 2017; Jing et al., 2018; Cusack et al., 2020).

Our frequency-based definition of mesoscale and submesoscale motions is designed by reference to frequency spectra of KE measured by the OSMOSIS moorings, an example of which is shown in Figure 2b. While there are some variations in the frequency partitioning of KE with depth and season (not shown), all spectra have a number of features in common that are typical of KE spectra across much of the global ocean (Ferrari and Wunsch, 2009), namely: a quasi-monotonic increase in KE with decreasing frequency, punctuated by local peaks at the semidiurnal (M_2) tidal frequency,

its M_4 harmonic, and the inertial frequency, as well as by a broad 'shoulder' at frequencies of $< 8 \times 10^{-3}$ cyc h^{-1} (approximately corresponding to periods of > 5 days) associated with mesoscale flows. Since this work is solely concerned with subinertial motions, we notionally exclude near-inertial and superinertial flows by setting the high-frequency boundary of the submesoscale band at the frequency of the subinertial spectral minimum, $\omega = 4.2 \times 10^{-2}$ cyc h^{-1} (corresponding to a period of 1 day, or approximately one and a half times the inertial period). In turn, the boundary between mesoscale and submesoscale motions is established by the abrupt change in spectral slope that occurs at the high-frequency flank of the mesoscale shoulder (Callies et al., 2020), which we identify with a frequency of $\omega = 8 \times 10^{-3}$ cyc h^{-1} (corresponding to a period of 5 days and a horizontal scale of ~ 20 km, where this distance was determined via a frequency-resolved structure function analysis (Callies et al., 2020)). The mesoscale band is assumed to span all sampled frequencies lower than this value (i.e. down to semi-annual). Although the choice of the boundary between mesoscale and submesoscale motions is subject to some ambiguity, our diagnostics of Π_ω are qualitatively insensitive to reasonable perturbations to that boundary – as well as to other sources of uncertainty in the calculation in (1). See Appendix A for a quantitative assessment of these uncertainties. In section 3, we will also examine Π_ω at lower (mesoscale) frequencies than that of the submesoscale - mesoscale boundary, in order to place our results in the context of previous investigations of the inverse KE cascade at mesoscale eddy scales (e.g., Scott and Wang, 2005; Tulloch et al., 2011; Arbic et al., 2013, 2014).

The computation of Π_ω for each frequency ω_i is performed by applying a fourth-order Butterworth filter with a cut-off of ω_i to the (gridded observational, or model) data. In the observational case, horizontal gradients are calculated using finite-difference methods applied to each of 30 triplet / quadruplet combinations of horizontal velocities from inner (or outer) moorings, followed by averaging of horizontal gradient estimates from individual inner-mooring (or outer-mooring)

combinations. The results of all calculations presented here are robust to the choice of computational approach (i.e. all possible triplet / quadruplet combinations of horizontal velocities yield similar diagnostics).

3. Results

Our assessment of cross-scale KE transfers in the OSMOSIS area is presented in three stages. First, observational diagnostics of Π_ω are documented at face value (section 3a), momentarily setting aside caveats stemming from their marginal statistical significance. Second, these caveats are quantified and discussed (section 3b), and the reader is invited to regard our observational results with caution. Third, diagnostics of Π_ω in the LLC4320 model are provided to: (i) gain further insight into sampling uncertainties potentially affecting our observational results; and (ii) identify similarities and differences with the observations that may point to model strengths and weaknesses (section 3c).

a. Observational estimates of cross-scale KE transfers

The evolution of the mesoscale and submesoscale classes of KE (as defined in section 2c) over the annual cycle sampled by the OSMOSIS moorings is shown in Figures 3b-c, contextualised with the mixed layer depth (contours) and the depth-integrated subinertial KE (Fig. 3a). As expected from the frequency spectra of KE in our study area (Fig. 2b) and elsewhere (Ferrari and Wunsch, 2009), mesoscale flows are substantially more energetic than submesoscale motions, typically by a factor of 2 - 4 and occasionally by as much as an order of magnitude. The two flow classes exhibit broadly similar temporal changes, but their vertical structures are distinct (cf. Figs. 3d and 3e). Mesoscale flows are characteristically intensified near the surface and display only a gentle reduction in their KE with depth. In contrast, submesoscale motions are most energetic

within and near the base of the mixed layer, and decay comparatively rapidly with depth. This difference in vertical structure qualitatively conforms to expectations from (linear and nonlinear) instability theory-based descriptions of mesoscale and submesoscale flows (Haine and Marshall, 1998; Fox-Kemper et al., 2008; Tulloch et al., 2011; Callies and Ferrari, 2013; Callies et al., 2015, 2016).

Both mesoscale and submesoscale motions are relatively quiescent during autumn, when the mixed layer deepens as a result of vigorous wind forcing and atmospheric cooling (Thompson et al., 2016; Buckingham et al., 2019). As winter sets in, mesoscale and submesoscale flows are intermittently energised by up to one order of magnitude, and persist in that invigorated state during the wintertime period of pronounced fluctuations in the mixed layer depth and the springtime phase of rapid upper-ocean re-stratification. A generally inactive summer follows, punctuated by two high-KE events in August - September. Overall, the seasonal pattern of mesoscale KE measured by the OSMOSIS moorings – with energy levels increasing through winter and peaking in late spring – is characteristic of the climatological annual cycle in the Northeast Atlantic as documented by altimetry (see e.g., Fig. 3a), as well as of the seasonal evolution of the mesoscale eddy field in other mid-gyre regions across the global ocean (Zhai, 2017).

The time series of cross-scale KE transfer between mesoscale and submesoscale motions (Fig. 4a) follows broadly the seasonal evolution of KE, with elevated and highly intermittent values of Π_ω at times of intensified mesoscale and submesoscale flows, particularly in winter and spring. During these periods, Π_ω regularly attains a magnitude on the order of 10^{-7} m^2 s^{-3} that is comparable to the local rates of change of the mesoscale and submesoscale classes of KE (Figs. 4c-d), suggesting that cross-scale KE transfers are a significant driver of the annual cycle of mesoscale and submesoscale

flows[1]. The sense of this driving, however, is not uniform throughout the year, but rather reverses in March, around the transition between winter and spring (Fig. 4a). Whereas during winter KE transfers toward lower frequencies (i.e. upscale, from submesoscale to mesoscale), in spring the KE transfer is directed toward higher frequencies (i.e. downscale, from mesoscale to submesoscale). Notably, these two distinct stages of cross-scale KE transfer are characterized by different vertical structures (Fig. 4e). Upscale KE transfers in winter are focussed in or near the mixed layer, and decrease to near-zero values well below the mixed layer base. Conversely, downscale KE transfers in spring regularly exhibit non-zero values over the entire water column segment measured by the OSMOSIS moorings.

A succinct overview of the annual cycle of KE transfers between mesoscale and submesoscale motions is obtained by cumulatively integrating Π_ω with time at each depth in the OSMOSIS data set (Fig. 4b). This perspective emphasizes the progressive effects of the intermittent, short-lived, high-transfer events that dominate Figure 4a. The two-stage nature of the annual cycle of cross-scale KE transfer, and the distinct vertical structure characteristic of each stage, are now obvious. A net upscale KE transfer occurs within the mixed layer from mid November and peaks in late February. There is little cross-scale KE transfer beneath the mixed layer base during this period. In contrast, a net downscale KE transfer occurs at all depths from March, peaking in late June. The net downscale KE flux in spring is largest in the uppermost 200 m, i.e. at depths encompassed by the winter mixed layer, but is also substantial at depths below the winter mixed layer base. Note that, while the broad magnitude and spatio-temporal structure of the cross-scale KE transfer displayed in Figures 4a-b are robust to analysis choices, the sign of the net, annually-integrated

[1]A close match between the temporal evolutions of the local rate of change of mesoscale (or submesoscale) KE and of Π_ω is not expected because the first of these terms is likely to be dominated by spatial transports of KE, with further contributions from forcing, conversion of potential to KE, and dissipation (see equation (6) in Aluie et al. (2018)).

downscale KE transfer apparent in Figure 4b is not robust (see discussion of Figure 5 below). Thus, our diagnostics indicate that the wintertime upscale and springtime downscale stages of the annual cycle of Π_ω are associated with KE transfers of the same order, but we are unable to confidently determine the sign of their residual.

A final point of note in our results concerns the frequency ranges acting as sources and sinks of the KE transferred upscale in winter, and of the KE transferred downscale in spring. Examination of Figure 5, showing Π_ω at the illustrative depth of 140 m as a function of frequency, reveals a systematic difference between the two stages of cross-scale KE transfer[2]. Upscale KE transfer events in winter operate across all resolved subinertial frequencies (as low as $\sim 3\times10^{-7}$ cyc s^{-1}, equivalent to periods as long as ~ 40 days), and typically peak at a frequency of $\sim 10^{-6}$ cyc s^{-1} (a period of ~ 10 days). This indicates that the wintertime upscale KE transfer activates the entire submesoscale range, and that it entails a net transfer of KE to mesoscale eddies with periods longer than ~ 10 days. In contrast, downscale KE transfer events in spring act primarily at frequencies higher than $\sim 5\times10^{-7}$ cyc s^{-1} (periods shorter than ~ 20 days), and typically peak at a frequency of $\sim 2\times10^{-6}$ cyc s^{-1} (a period of ~ 5 days). This suggests that the springtime downscale KE transfer does not substantially drain the bulk of the mesoscale range, but mainly fluxes KE across the mesoscale - submesoscale boundary. At periods longer than ~ 20 days, upscale KE transfers are generally prevalent throughout the year, as expected from the occurrence of an inverse KE cascade over the low-horizontal-wavenumber mesoscale range previously documented in altimetric observations (Scott and Wang, 2005; Tulloch et al., 2011). The local presence in the OSMOSIS region of such an inverse KE cascade in horizontal wavenumber space has been confirmed here through analysis of the altimetric measurements (not shown).

[2]Two semi-independent estimates of Π_ω are presented, based on horizontal velocity gradients computed from either the inner moorings (Figs. 5a,c) or the outer moorings (Figs. 5b,d), in order to illustrate the robustness to analysis choices of the key diagnostics discussed here.

b. Robustness of observational estimates of cross-scale KE transfers

As advanced in section 3a, our central result of the occurrence of two seasonal stages – of comparable magnitude and distinct vertical structure – in the KE transfer between mesoscale and submesoscale flows at the OSMOSIS site is stable for the location and period measured by the mooring array. This is demonstrated through an analysis of the uncertainties introduced in our estimate of Π_ω by the non-trivial (horizontal and vertical) motion of the moorings, and instrumental errors. This analysis is detailed in Appendix A, and concludes that all the salient cross-scale KE transfer events in Figure 3a, and their seasonally integrated effects in Figure 3b, are qualitatively insensitive to such sources of error, with corresponding quantitative uncertainties on the order of 10%.

An additional source of error in our Π_ω diagnostics stems from the moorings' sub-optimal sampling of the spatio-temporally complex flow field, linked to the limited horizontal resolution (which restricts estimation of the low-frequency lateral gradients in (1) to a small set of resolved horizontal distances) and extent (1 year, which encompasses a relatively modest number of (sub-)mesoscale eddy events) of the measurements. In order to probe this sampling uncertainty, we perform an array of alternative calculations of Π_ω, founded on synthetic time series of horizontal velocity that have the same amplitudes as in the observations but (on average) zero cross-scale KE transfers (Appendix C). This assessment suggests that, despite its dynamical plausibility (section 4a) and consistency with model results (section 3c), the wintertime upscale KE transfer may stem from sampling issues. Although the springtime downscale KE transfer is robust to such issues, clearly there are elements of our KE transfer diagnostics that lie at the margins of statistical significance – so our observational results must be treated cautiously.

The limiting influence of sampling errors is also apparent in our estimates of cross-scale KE transfers at frequencies other than that of the submesoscale - mesoscale boundary (Fig. 5), which inform our characterization of the scales acting as sources and sinks of the wintertime upscale KE transfer and springtime downscale KE transfer across that boundary. Calculations of Π_ω reliant on horizontal gradients computed from the inner moorings (Fig. 5a) and from the outer moorings (Fig. 5b) generally agree on the temporal and frequency distributions of the KE transfer, although the magnitude of outer mooring-based diagnostics is typically reduced relative to that of inner mooring-based diagnostics by a factor of 2-3. These quantitative differences can, at times, result in the two estimates of the time-integrated KE transfer acquiring opposite signs (e.g., in spring; cf. Figs. 5c and 5d). Such an issue, however, affects only relatively low frequencies in the mesoscale range (periods longer than ~ 5 days, which have the lowest number of degrees of freedom in the OSMOSIS record) and is ephemeral, so that the sign of the annually-integrated KE transfer is widely consistent between outer and inner mooring-based diagnostics.

All in all, a recurrent feature of our Π_ω estimates is their reduced robustness as longer-time-scale effects are considered. Such effects result from the imperfect cancellation between large, oppositely-signed KE transfers, and are thereby expected to be especially sensitive to sampling uncertainties. A more comprehensive characterization of the sampling errors in our observational estimates of Π_ω will be provided in section 3c, by reference to the LLC4320 simulation.

c. Cross-scale KE transfers in the LLC4320 model

We next compute the annual cycle of cross-scale KE transfers in the LLC4320 simulation, by applying the same methodology as that of the observational analysis at each model grid point within a 290 km $\times$ 260 km area encompassing the OSMOSIS mooring site (Fig. 1a). The rationale of this model-based computation is two-fold. First, consideration of a wider area instead of a small

cluster of model grid points (which would be more akin to the mooring observations) enables us to further assess how sampling limitations may influence our observational diagnostics. As indicated in section 3b, such limitations may be non-trivial, given the moorings' finite sampling capability and the expected spatio-temporal patchiness of the KE transfer field (see e.g., the model-based calculation by Schubert et al. (2020)). Second, assessment of KE transfers in the LLC4320 simulation allows us to evaluate its degree of agreement with mooring-based results, and thereby provides a window into the strengths and weaknesses of state-of-the-art, submesoscale-permitting ocean models. Note that, as outlined in section 2b, the model and observations span different years (2011-2012 and 2012-2013, respectively), so that our model-observations comparison rests on the assumption that both years are widely representative.

The annual cycles of the spatially-averaged mesoscale KE, submesoscale KE, KE transfer between mesoscale and submesoscale motions, and time-integrated KE transfer in the model are respectively shown in Figures 6a-d. The magnitudes, annual evolutions and vertical structures of the modeled mesoscale and submesoscale KE classes (Figs. 6a-b,e-f) are broadly in line with the OSMOSIS observations (Fig. 3b-e), with generally elevated KE levels in winter and spring in both data sets. There is, however, a non-trivial distinction between the model and the observations. While in the latter mesoscale and submesoscale motions are energized quasi-concurrently throughout the year, the springtime invigoration of mesoscale flows in the model appears to continue into the summer over 1-2 months after submesoscale motions have decayed. This points to a significant difference between the modeled and observed cross-scale KE transfers, which we elicit next through direct inspection of such transfers.

As for the observations (Fig. 4a), the cross-scale KE transfer in the model (Fig. 6c) is near-zero in the summer and early autumn, and is predominantly upscale in winter, when it occurs at a characteristic, surface-intensified rate regularly approaching 10^{-7} m^2 s^{-3}. Yet, unlike for the

observations, the modeled cross-scale KE transfer continues to be primarily upscale in spring. Although there are indications of a few weak ($O(10^{-8}$ m^2 s^{-3})), deep-penetrating events of downscale KE transfer qualitatively reminiscent of those in the measurements, the model's cross-scale KE transfer in spring is statistically indistinguishable from that in winter. The persistence of upscale KE transfers into spring results in the model hosting an annually-integrated inverse KE cascade (Fig. 6d), whereby submesoscales systematically energize the mesoscale eddy field throughout winter and spring. While this finding is in accord with previous analyses of cross-scale KE transfers in submesoscale-permitting models (Sasaki et al., 2014, 2017; Uchida et al., 2017; Klein et al., 2019; Dong et al., 2020), it stands in contrast with the more nuanced observational picture described earlier in our work – in which submesoscales may both supply and drain mesoscale KE at distinct stages of the annual cycle (Fig. 4b). The model (Fig. A2) and observations (Fig. 5) do agree, however, in indicating the occurrence of an inverse KE cascade across the bulk of the mesoscale range, in line with findings from mesoscale-resolving models (Arbic et al., 2013, 2014) and altimetric measurements (Scott and Wang, 2005; Tulloch et al., 2011).

In order to assess the robustness of the model - observations similarities and differences to measurement sub-sampling issues, we examine the spatial patchiness of the model's KE transfer between mesoscale and submesoscale flows within the domain analyzed (Fig. 7). Inspection of maps of the wintertime (Fig. 7a) and springtime (Fig. 7b) cross-scale KE transfers reveals that there is substantial inhomogeneity in the distribution of Π_ω, with downscale KE transfers prevailing in some areas of horizontal extent comparable to that of the OSMOSIS mooring array in both seasons. Note, however, that only 11.6% of model grid points exhibit both wintertime upscale and springtime downscale KE transfers, i.e. a seasonal cycle of the cross-scale KE transfer in accordance with our mooring-based diagnostics. A direct quantitative comparison of the observational and model-derived estimates of the cross-scale KE transfer is provided by Figures

7c,d, which respectively display the observational winter-mean and spring-mean values of Π_ω in the context of the probability distribution functions of the model's KE transfer in each season. This comparison demonstrates that, while observations and model are not inconsistent in winter, they are unambiguously incompatible in spring, when the observational season-mean Π_ω is more strongly downscale than the KE transfer in any model grid point.

4. Discussion

Next, we discuss our findings on the KE transfers between mesoscale and submesoscale motions in two steps. First, we consider the physical processes potentially implicated in the cross-scale KE transfers – briefly disregarding reservations on the statistical significance of the KE transfer diagnostics – to suggest that the upscale and downscale transfer stages are underpinned by distinct dynamics. Second, we draw on our assessment of cross-scale KE transfers in the LLC4320 simulation, in comparison to observational results, to extract lessons for the representation of mesoscale - submesoscale interactions in ocean models.

a. Dynamics of KE transfers between mesoscale and submesoscale motions

We now explore the physical processes underpinning each of the two seasonal stages of the KE transfer between mesoscale and submesoscale motions, assuming for the sake of discussion that both stages are genuine and not a statistical artifact – the latter being a possibility that we cannot definitively discount. Although this assessment is far from conclusive (due to the finite length of the observational record and the unavailability of measurements of some relevant variables, such as vertical velocity within the mixed layer), the OSMOSIS observations contain sufficient information to suggest plausible dynamical interpretations of each seasonal KE transfer

stage. These interpretations will be tested against the LLC4320 simulation, and used to elucidate characteristic model strengths and weaknesses, in section 4b.

An overview of the wintertime upscale KE transfer and its dynamical context is provided by Figure 8. Upscale KE transfers are now clearly seen to occur in the form of short-lived events (indicated by blue arrows in the upper axis) with a magnitude of O(10^{-7} m^2 s^{-3}) and a typical duration of a few days (Fig. 8a), clustered in several periods in December to February. Clusters of upscale KE transfer events are interspersed with longer episodes of near-zero KE transfer, which are sometimes punctuated by ephemeral instances of downscale KE transfer. Close inspection of the evolution of the mixed layer depth indicates that upscale KE transfer events regularly follow rapid mixed layer shoaling (e.g., the second and fourth events), and that, in contrast, little KE transfer occurs when the mixed layer is consistently deeper than in preceding or subsequent periods (e.g., between the second and third events, or between the third and fourth events).

The processes behind this correspondence between the directionality of the cross-scale KE transfer and the mixed layer's behaviour are illuminated by Figures 8b,c, which respectively show the vertical buoyancy flux $w'b'$ (i.e. the rate of re-stratification; where w is the vertical velocity, b is buoyancy, and primes represent perturbations relative to a temporal mean) below the mixed layer base (Su et al., 2018; Yu et al., 2019b) and the potential vorticity ($q = (f\mathbf{k} + \nabla \times \mathbf{u}) \cdot \nabla b$; where $\mathbf{k}$ is the vertical unit vector, ∇ is the 3-d spatial gradient operator, and $\mathbf{u}$ is the 3-d velocity), negative values of which (strictly, $fq < 0$) indicate conditions favourable to the development of submesoscale gravitational and symmetric instabilities (Thomas et al., 2013; Thompson et al., 2016; Buckingham et al., 2020; Yu et al., 2021). Both $w'b'$ and q are diagnosed from the OSMOSIS mooring observations, as described by Yu et al. (2019b, 2021). Briefly, w is assessed by applying the mass conservation equation after neglecting the diffusion term, and is thus available only below the strongly diabatic mixed layer. w' and b' are respectively computed as deviations from 10-day

running means of w and b, with this time scale selected to span the decorrelation scales of both variables. See section 2c in Yu et al. (2019b) for a more detailed justification of these analytical choices.

Periods of near-zero or weakly downscale KE transfer and a depressed mixed layer base are commonly associated with negative q values conducive to the onset of gravitational and symmetric instabilities (blue shading in Figure 8c), which sequentially induce a deepening and shoaling of the mixed layer in response to intense wind and buoyancy forcings (Thompson et al., 2016; Yu et al., 2021). Immediately after this forcing ceases, and just as upscale KE transfer ensues, q becomes positive (red shading in Figure 8c) and further re-stratification occurs, evidenced by both a contracting mixed layer and positive vertical buoyancy fluxes below the mixed layer (red shading in Figure 8b). The relationship between upscale (i.e. negative) KE transfers and re-stratifying (i.e. positive) vertical buoyancy fluxes is explicitly borne out by Figure 8d, which reveals a statistically significant anticorrelation ($r = -0.44$, $p < 0.05$) between the two variables in winter. This suite of dynamical signatures (positive potential vorticity, mixed layer shoaling, and re-stratifying vertical buoyancy fluxes) are suggestive of the occurrence of mixed-layer baroclinic instability (Boccaletti et al., 2007; Fox-Kemper et al., 2008; Thompson et al., 2016), whereby overturning motions effect a slumping of submesoscale upper-ocean fronts by tilting steeply-sloping buoyancy surfaces toward the horizontal[3]. The existence of a significant positive correlation between the vertical buoyancy flux and the intensity of submesoscale upper-ocean fronts (Yu et al., 2019b) is consistent with this interpretation, although some involvement of mesoscale frontogenesis in triggering re-stratification is also likely and may contribute to the scatter in Figure 8d.

[3]Note that, while both symmetric and mixed-layer baroclinic instabilities may develop concurrently under $fq < 0$ conditions, the dominance of baroclinic instability characteristically emerges only as fq adopts positive values, due to this instability's slower growth (Stamper and Taylor, 2016).

An illustration of the springtime downscale KE transfer and its dynamical context is provided by Figure 9. Downscale KE transfer events of O(10^{-7} m^2 s^{-3}) occur in three typically week-long main clusters in early March, mid-to-late March (marked by red arrows in the upper axis of Figure 9a) and mid April (Fig. 4a). After mid April, the cross-scale KE transfer is near-zero, with the exception of an isolated episode of downscale transfer in June (Fig. 4a). In contrast to winter, events of large KE transfer in spring extend to the deepest instrumented level of the moorings rather than being focussed in the mixed layer (Fig. 4a). This suggests that the springtime downscale KE transfer is primarily driven by mesoscale processes which, unlike submesoscales, are associated with horizontal velocity variability with low-wavenumber vertical structure (de La Lama et al., 2016).

In order to constrain the controlling mesoscale processes, Figures 9b,c respectively display the submesoscale horizontal buoyancy gradient (measuring the strength of fronts on the horizontal scale of the inner-mooring side length, i.e. 2.5 km) and the mesoscale frontogenesis function (F_S, a measure of the rate at which confluent mesoscale flow intensifies horizontal buoyancy gradients). F_S is calculated following the expression (Hoskins, 1982):

$$F_S = -(\partial_x \mathbf{u_h} \cdot \nabla_\mathbf{h} b, \partial_y \mathbf{u_h} \cdot \nabla_\mathbf{h} b) \cdot \nabla_\mathbf{h} b, \tag{2}$$

where horizontal gradients of $\mathbf{u_h}$ and b are computed from 30-h low-pass filtered outer-mooring measurements (see Yu et al. (2019b) for a full account of this calculation). Clusters of downscale KE transfer events regularly correspond with periods of elevated frontogenesis (Fig. 9c), which induce a sharpening of lateral buoyancy gradients (Fig. 9b) (Yu et al., 2019b). Such preferential occurrence of downscale (i.e. positive) KE transfers at times of intensified frontogenetic tendencies and lateral buoyancy gradients is shown explicitly in Figure 9d, which captures the statistically significant correlation ($r = 0.43$, $p < 0.01$) between the two variables in spring. (Note that Figure

9d uses positive values of F_S, in order to distinguish frontogenetic events from frontolytic scenarios that often occur in close mutual proximity (e.g., Fig. 9c); however, considering the magnitude of F_S instead does not significantly alter the histogram in Figure 9d.) The characteristic decay of the lateral buoyancy gradients below the mixed layer suggests that they are associated with submesoscale upper-ocean fronts. Thus, a possible interpretation of this set of diagnostics is that downscale KE transfers in spring are effected by deep-reaching frontogenetic mesoscale flows straining submesoscale upper-ocean fronts. Such straining action is expected to result in a rapid filamentation of submesoscale frontal features, sharpening lateral buoyancy gradients and producing buoyancy variance at increasingly higher horizontal wavenumbers (Capet et al., 2008a; Barkan et al., 2019; Siegelman, 2020). These conditions have been shown to favour the onset of loss of balance and generation of the divergent, ageostrophic motions required to drive a downscale KE transfer (Capet et al., 2008b; Molemaker et al., 2010; Molemaker and McWilliams, 2010; Barkan et al., 2015; Poje et al., 2017; Schubert et al., 2020). The association between downscale KE transfers and mesoscale frontogenesis suggested here may be bolstered by the enhancement of re-stratification documented during frontogenetic events (Yu et al., 2019b), which is expected to convert mesoscale potential energy to submesoscale KE at those times.

To summarize, our exploratory assessment of the dynamics regulating the annual cycle of the KE transfer between mesoscale and submesoscale motions suggests the following picture. In the summer and early autumn, mesoscale and submesoscale eddy activity is generally weak, and there is little KE transfer between the two classes of flow. Later in autumn and into winter, intense wind and buoyancy forcings regularly generate gravitational and symmetric instabilities at the weak submesoscale upper-ocean fronts dotted across the area. Although these instabilities drive an overall deepening of the mixed layer (Yu et al., 2021), rapid re-stratification and upscale KE transfer occur – most likely as a result of mixed-layer baroclinic instability – at times of modest forcing.

In this way, submesoscale motions energize mesoscale flows during winter. As spring arrives, the newly-invigorated mesoscale eddy field – now close to reaching its annual KE maximum (Fig. 3b) – induces episodes of frontogenesis, during which submesoscale upper-ocean fronts may be strained into progressively smaller structures, plausibly giving rise to a downscale KE transfer. Thus, while in spring the inverse KE cascade initiated by submesoscales in winter may continue over the bulk of the mesoscale range (Fig. 5), some mesoscale KE can be lost back to submesoscales, thereby contributing to sustaining a submesoscale eddy field into summer.

b. Insights into the representation of mesoscale - submesoscale interactions in ocean models

Having established the key points of agreement and disagreement between the LLC4320 simulation and the OSMOSIS observations in section 3c, we turn to the question of what processes underpin such similarities and differences. Considering similarities first, the model endorses our observation-based, mechanistic interpretation of upscale KE transfers being significantly driven by mixed-layer baroclinic instability. This is illustrated by Figure 10, which displays the time series of the vertical buoyancy flux (Fig. 10a) and the relationship between this flux and the cross-scale KE transfer (Fig. 10b) in the model. As suggested by observational results (Fig. 8), periods of modeled upscale KE transfer (Fig. 6c) are commonly characterized by re-stratifying vertical buoyancy fluxes focused within and around the base of the mixed layer (Fig. 10a), which are the hallmark signature of mixed-layer baroclinic instability (Boccaletti et al., 2007; Fox-Kemper et al., 2006; Thompson et al., 2016). Although there is substantial scatter in the relationship between the vertical buoyancy flux and Π_ω, instances of elevated upscale KE transfer (e.g., $\Pi_\omega < 3\times10^{-8}$ m^2 s^{-3}) are systematically associated with events of intense re-stratification ($w'b' > 10^{-8}$ m^2 s^{-3}). The scatter in Figure 10b is unsurprising, as the vertical buoyancy flux and Π_ω may not necessarily change concurrently. For example, re-stratification could in principle occur without any simulta-

neous upscale KE transfer, and such transfer could take place at a later stage through the merging of mixed-layer eddies. Thus, we surmise that the model's ability to reproduce KE transfers from submesoscale to mesoscale motions rests on its adequate representation of the effects of mixed-layer baroclinic instability. This result is expected from the model's submesoscale-permitting resolution (Su et al., 2018), and is in line with previous investigations of cross-scale KE transfers in submesoscale-permitting models (Sasaki et al., 2014, 2017; Uchida et al., 2017; Klein et al., 2019; Dong et al., 2020; Schubert et al., 2020).

Why, then, does the LLC4320 model largely fail to simulate the springtime KE transfer from mesoscale to submesoscale flows diagnosed in observations? Our analysis indicates that a plausible explanation is the model's muted representation of the mechanism arguably responsible for the direct KE transfer: the straining of submesoscale upper-ocean fronts by frontogenetic mesoscale motions (see section 4a). As demonstrated by Figure 11, the frontogenetic tendency (quantified by positive values of the frontogenesis function, F_S) of modeled mesoscale flows (Fig. 11b) is considerably lower than observed (Fig. 11a), by typically half an order of magnitude. This results in submesoscale lateral buoyancy gradients that are unrealistically weak in the model, by at least half an order of magnitude too (cf. Figs. 11a-b). Invoking thermal wind, such subdued filamentation of submesoscale frontal features must reduce the downscale KE transfer out of the mesoscale range (e.g., Capet et al., 2008a,b; Barkan et al., 2015, 2019; Schubert et al., 2020), leaving the modeled mesoscale eddy field to evolve unimpeded and transfer KE upscale. We thus suggest that the enhanced persistence of elevated mesoscale KE in spring / summer in the LLC4320 simulation most likely stems from the model's sub-optimal representation of frontogenetically-driven downscale KE transfers in spring. In accord with this suggestion, the model reproduces a significant springtime association between large positive values of the frontogenesis function and weak downscale KE transfers (Figs. 12a-b,d), but this manifests at periods considerably shorter

than that of the mesoscale - submesoscale boundary (i.e. at periods of $\sim$ 1 day, and not 5 days; cf. Figs. 12b,c and 12d,e).

Our inference that mesoscale frontogenesis and submesoscale fronts are excessively dampened in the model is consistent with the structure function diagnostics of Erickson et al. (2020). These reveal that, while mesoscale KE levels in the LLC4320 simulation are broadly realistic, lateral buoyancy gradients are too weak in the model (which has a horizontal grid spacing of $\sim$ 2 km in the OSMOSIS region) across horizontal scales of O(1-10 km) and, increasingly, on horizontal scales below 5 km characteristic of submesoscale fronts (see also the analogous conclusion reached by Cao et al. (2019)). Such model limitation conforms to the expected footprint of the model's grid-scale diffusive mixing eroding scalar gradients on horizontal scales smaller than about 6-7 grid spacings (Soufflet et al., 2016). The generality of our finding of a frontogenesis-induced downscale KE transfer with acute sensitivity to model resolution is suggested by Schubert et al. (2020), who reported the occurrence of such a transfer in submesoscale-permitting simulations of the Agulhas region. We conjecture that their model's ability to more clearly capture frontal downscale KE transfers stems from its finer horizontal resolution (down to $1/60^{\circ}$) compared to the LLC4320 simulation, as well as from their domain's lower latitude and enhanced stratification (yielding a substantially larger mixed-layer Rossby radius) relative to the OSMOSIS area.

5. Conclusions

In this work, we have performed the first observational assessment of the annual cycle of the KE transfer between mesoscale and submesoscale motions (respectively characterized by time scales longer and shorter than 5 days, equivalent to horizontal scales larger and smaller than $\sim$ 20 km; Callies et al., 2020) in the upper layers of a typical mid-ocean region, using a unique mooring data set that resolves and spans the fundamental spatio-temporal scales of both classes of flow.

Although our diagnostics have marginal statistical significance at best and should thus be regarded cautiously, they are physically plausible and can provide a valuable benchmark against which to evaluate model-based findings.

Such caveats considered, our key result is that the cross-scale KE transfer exhibits two distinct seasonal stages, whereby submesoscales energize the mesoscale eddy field (an upscale KE transfer) in winter and drain energy from mesoscales (a downscale KE transfer) in spring. Despite the diagnosed seasonal reversal in the mesoscale - submesoscale KE transfer, an inverse KE cascade is found to operate throughout the year across the bulk of the mesoscale range (on time scales longer than ~ 20 days, or horizontal scales larger than ~ 40 km; Callies et al., 2020), in accord with previous diagnostics from altimetric measurements of those coarse scales (Scott and Wang, 2005; Tulloch et al., 2011). All in all, our results are not incompatible with a body of recent submesoscale-permitting modeling work (Sasaki et al., 2014, 2017; Uchida et al., 2017; Klein et al., 2019; Dong et al., 2020) that: (i) places the headwaters of the inverse KE cascade at the submesoscale; and (ii) rationalizes the widely observed seasonal cycle in mesoscale KE (Zhai, 2017) as an inverse cascade-mediated response to the generation of submesoscale KE in winter. However, our findings also challenge those investigations by suggesting that, in spring, KE transfers across the mesoscale - submesoscale boundary can act to dampen (rather than invigorate) the inverse KE cascade – a result that resonates with cross-scale KE transfer diagnostics in theoretical studies of idealized flows in turbulent equilibrium (Molemaker et al., 2010; Molemaker and McWilliams, 2010; Barkan et al., 2015; Brüggemann and Eden, 2015), in realistic numerical models of frontogenetic flows (Capet et al., 2008a,b; Schubert et al., 2020), and in analyses of ocean surface drifter observations (Poje et al., 2017).

An appraisal of the candidate dynamics most likely to govern the observed seasonal cycle of the mesoscale - submesoscale KE transfer indicates that the winter and spring transfer stages are

underpinned by distinct processes. Consistent with results from submesoscale-permitting models, the wintertime upscale KE transfer may be associated with mixed-layer baroclinic instability, which induces re-stratification by slumping submesoscale upper-ocean fronts (Boccaletti et al., 2007; Fox-Kemper et al., 2008; Thompson et al., 2016; Yu et al., 2019b) following instances of de-stratifying atmospheric forcing. In contrast, the springtime downscale KE transfer is suggestively linked to the filamentation of submesoscale upper-ocean fronts by frontogenetic mesoscale motions that have been previously energized by the wintertime upscale KE transfer. We thus contend – on the basis of these inferences, and to the extent that our findings may be robust and more widely representative – that the state-of-the-art, submesoscale-permitting models providing the grounding for recent views of a winter submesoscale-initiated inverse KE cascade (Sasaki et al., 2014, 2017; Uchida et al., 2017; Klein et al., 2019; Dong et al., 2020; Schubert et al., 2020) adequately capture the key KE transfer effects of mixed-layer baroclinic instability, but could substantially understate the impacts of frontogenetic processes.

We propose that resolving this potential limitation of the current generation of high-resolution ocean circulation models (by e.g., refining resolution) may result in two significant changes to the models' perspective on the ocean's energy cycle. First, the submesoscale-induced invigoration of the mesoscale eddy field is likely to be increasingly focussed to winter, with frontogenetic processes in spring acting to temper (rather than further promote) the inverse KE cascade. Second, direct KE transfers elicited by such frontogenetic processes might be expected to prolong the energized wintertime state of the submesoscale eddy field further toward, or into, summer. Capturing these changes is likely to require model resolutions approaching O(100 m) in the horizontal (e.g., Brannigan et al., 2015; Schubert et al., 2020), and may arguably have notable consequences for all aspects of ocean circulation shaped by (sub-)mesoscale eddy transports.

Acknowledgments. The OSMOSIS experiment was funded by the U.K. Natural Environment Research Council (NERC) through grants NE/1019999/1 and NE/101993X/1. ACNG acknowledges the support of the Royal Society and the Wolfson Foundation, and XY that of a China Scholarship Council PhD studentship. We are grateful to the engineers, scientists, captain and crew of the RRS Discovery, RRS James Cook, and R/V Celtic Explorer, who participated in the deployment and recovery of the moorings and gliders. All data are archived at the British Oceanographic Data Centre. We thank Zachary Erickson and Andrew Thompson for providing us with the LLC4320 model output, and Baylor Fox-Kemper, Hemant Khatri and three anonymous reviewers for insightful feedback.

Data availability statement. All OSMOSIS mooring and glider data are freely available, are stored in an accessible data format, contain metadata, and can be obtained from the British Oceanographic Data Centre (https://www.bodc.ac.uk). The LLC4320 simulation data can be directly accessed from the ECCO Data Portal (https://data.nas.nasa.gov/ecco/data.php).

APPENDIX A

Observational uncertainty in the cross-scale KE transfer

We quantify the observational uncertainties in our Π_ω diagnostics introduced by two sources of error: mooring motion, and instrumental errors in the horizontal velocity measurements.

First, because the estimation of Π_ω entails horizontal gradients computed from mooring-based horizontal velocity measurements, unknown mooring motions could result in uncertainty in the locations of the measurements. Stochastic modeling predicts that horizontal displacements rarely exceed 500 m (Buckingham et al., 2016). Following this work, we model inter-mooring distance perturbations associated with mooring motion as a Gaussian white noise process with zero mean and non-zero variance, estimated from the time integration of differential horizontal currents. Second, instrumental error arises from the finite accuracy of the moored sensors, and is unavoidable during the measuring process. According to manufacturer specifications, the precision of Nortek Aquadopp current meters is 0.005 m s^{-1} (https://support.nortekgroup.com/hc/en-us/articles/360029839351-The-Comprehensive-Manual-Velocimeters).

To estimate the total uncertainty due to these factors, we introduce random errors from the two sources simultaneously, and allow these errors to accumulate in the Π_ω estimates. In doing so, the errors associated with mooring motion and instrumental noise are assumed to be independent. This exercise is repeated 1000 times. An illustration of its outcome is provided by Figure A1, in which the modest influence of the observational uncertainties considered here can be appreciated. Π_ω diagnostics are qualitatively unaffected by these sources of error, both as regards the temporal evolution of Π_ω (cf. Figs. A1a,b) and its probability distributions in winter (Fig. A1c) and

spring (Fig. A1d). Quantitative perturbations to Π_ω introduced by observational uncertainties are typically $< 4 \times 10^{-8}$ m^2 s^{-3}, or on the order of 10% (cf. Figs. A1a,b).

APPENDIX B

Comparison of cross-scale KE transfer diagnostics in frequency and horizontal wavenumber in the LLC4320 simulation

Previous investigations of the cross-scale KE transfer in mesoscale-permitting or -resolving numerical models (Arbic et al., 2012, 2014; Sérazin et al., 2018; O'Rourke et al., 2018) suggest that the transfer's rate and direction in frequency space are generally in agreement with those in horizontal wavenumber space. This assertion is important to our work, since it underlies our discussion of the relationship between our KE transfer diagnostics (which are conducted in frequency space) and those of preceding studies (which are commonly formulated in horizontal wavenumber space). The expected basic equivalence between KE transfers in frequency and horizontal wavenumber spaces is corroborated here by computing both transfers in the OSMOSIS area in the LLC4320 simulation (see section 2b for a description of the model). The calculations are conducted at each temporal snapshot in the 14-month simulation for a range of frequencies and horizontal wavenumbers (respectively corresponding to periods of 1-30 days and horizontal scales of 6-50 km).

The resulting cross-scale KE transfers in frequency and horizontal wavenumber are compared in Figure A2. Although there are differences in the finer detail, both KE transfers exhibit:

- a predominantly upscale (negative) KE transfer of magnitude of O(10^{-8} m^{-2} s^{-3}) in winter and spring focussed on large scales (periods in excess of $\sim$ 5 days and horizontal scales greater than $\sim$ 20 km), with downscale (positive) transfers at smaller scales (cf. Figs. A2a and A2b);

- an enhancement of upscale (negative) KE transfers in spring relative to winter by less than a factor of 2 over a wide range of periods and horizontal scales (cf. Figs A2c and A2d).

Based on these results, we conclude that the assertion that KE will generally transfer toward slowly-evolving (rapidly-evolving) flows as it transfers toward flows with large (small) horizontal scales is likely to hold in the OSMOSIS region.

APPENDIX C

Statistical significance of observational diagnostics of cross-scale KE transfer

The cross-scale KE transfer between periods longer and shorter than 5 days (i.e. between mesoscales and submesoscales) is a third-order statistic, and depends on the phase relation between horizontal velocities and horizontal velocity gradients. The finite observational period limits the number of available degrees of freedom, particularly for the low-frequency flow. To assess the statistical significance of the Π_ω diagnosed from the observations, we here apply the KE transfer calculation to synthetic time series of horizontal velocity that have the same amplitudes as in the observations but randomized phases. On average, these synthetic time series thus have no KE transfer, and non-zero diagnosed transfers are the result of the limited sampling. We treat this zero-transfer case as the null hypothesis, and evaluate the significance at which we can reject it given the real time series.

To generate the randomized time series, we apply a discrete Fourier transform to the observed horizontal velocity time series at all moorings and at each depth. We randomize the phase of the Fourier coefficients by shifting each coefficient's phase by a random offset drawn from a uniform distribution between 0 and 2π. The same random offset is applied for both components of horizontal velocity, in order to preserve variances of vorticity, divergence, strain and other derived variables. To retain the magnitude of horizontal velocity gradients, we apply the same phase offset to all moorings. (Errors that are uncorrelated between moorings have a negligible impact on the KE transfer.) We then calculate the KE transfer across the 5-day period as before, and repeat for a total of 10^4 such randomized time series.

We assess the significance of a non-zero cumulative KE transfer over the full year as well as over the first and second halves of the year (respectively encompassing winter and spring) separately (Fig. A3). For the full year, the observed transfer falls into the 95% confidence interval of the null hypothesis at all depths. For the first half of the year, the observed value straddles the lower boundary of the confidence interval around a depth of 250 m, but otherwise squarely falls into that interval. For the second half of the year, the observed value straddles the upper boundary of the confidence interval over the full range of depths, indicating that the null hypothesis can be rejected in this case at about a 95% level. We thus surmise that the statistical significance of our diagnosed upscale KE transfer in winter is marginal, whereas that of the downscale KE transfer in spring is robust.

References

Aluie, H., M. Hecht, and G. K. Vallis, 2018: Mapping the energy cascade in the North Atlantic Ocean: The coarse-graining approach. *J. Phys. Oceanogr.*, **48**, 225-244.

Arbic, B. K., R. B. Scott, G. R. Flierl, A. J. Morten, J. G. Richman, and J. F. Shriver, 2012: Nonlinear cascades of surface oceanic geostrophic kinetic energy in the frequency domain. *J. Phys. Oceanogr.*, **42**, 1577-1600.

Arbic, B. K., K. L. Polzin, R. B. Scott, J. G. Richman, and J. F. Shriver, 2013: On eddy viscosity, energy cascades, and the horizontal resolution of gridded satellite altimeter products. *J. Phys. Oceanogr.*, **43**, 283-300.

Arbic, B. K., M. Müller, J. G. Richman, J. F. Shriver, A. J. Morten, R. B. Scott, G. Sérazin, and T. Penduff, 2014: Geostrophic turbulence in the frequency–wavenumber domain: Eddy-driven low-frequency variability. *J. Phys. Oceanogr.*, **44**, 2050-2069.

Arbic, B. K., and twenty-six others, 2018: A primer on global internal tide and internal gravity wave continuum modeling in HYCOM and MITgcm. In *New Frontiers In Operational Oceanography*, 307-391.

Ballarotta, M., C. Ubelmann, M.-I. Pujol, G. Taburet, F. Fournier, J.-F. Legeais, Y Faugere, A. Delepoulle, D. Chelton, and G. Dibarboure, 2019: On the resolutions of ocean altimetry maps. *Ocean Sci.*, **15**, 1091-1109.

Barkan, R., J. M. Molemaker, K. Srinivasan, J. C. McWilliams, and E. A. D'Asaro, 2019: The role of horizontal divergence in submesoscale frontogenesis. *J. Phys. Oceanogr.*, **49**, 1593-1618.

824 Barkan, R., K. B. Winters, and S. G. Llewellyn-Smith, 2015: Energy cascades and loss of balance
825 in a reentrant channel forced by wind stress and buoyancy fluxes. *J. Phys. Oceanogr.*, **45**, 272-293.
826
827 Barkan, R., K. B. Winters, and J. C. McWilliams, 2017: Stimulated imbalance and the enhancement
828 of eddy kinetic energy dissipation by internal waves. *J. Phys. Oceanogr.*, **47**, 181-198.
829 Boccaletti, G., R. Ferrari, and B. Fox-Kemper, 2007: Mixed layer instabilities and restratification.
830 *J. Phys. Oceanogr.*, **37**, 2228-2250.
831 Brannigan, L., D. P. Marshall, A. C. Naveira Garabato, and A. J. G. Nurser, 2015: The seasonal
832 cycle of submesoscale flows. *Ocean. Model.*, **92**, 69-84.
833 Brannigan, L., D. P. Marshall, A. C. Naveira Garabato, A. J. G. Nurser, and J. Kaiser, 2017:
834 Submesoscale instabilities in mesoscale eddies. *J. Phys. Oceanogr.*, **47**, 3061-3085.
835 Brüggemann, N., and C. Eden, 2015: Routes to dissipation under different dynamical conditions.
836 *J. Phys. Oceanogr.*, **45**, 2149-2168.
837 Buckingham, C. E., A. C. Naveira Garabato, A. F. Thompson, L. Brannigan, A. Lazar, D. P.
838 Marshall, A. J. G. Nurser, G. Damerell, K. J. Heywood, and S. E. Belcher, 2016: Seasonality of
839 submesoscale flows in the ocean surface boundary layer. *Geophys. Res. Lett.*, **43**, 2118-2126.
840 Buckingham, C. E., N. S. Lucas, S. E. Belcher, T. P. Rippeth, A. L. M. Grant, J. Le Sommer, A. O.
841 Ajayi, and A. C. Naveira Garabato, 2019: The contribution of surface and submesoscale processes
842 to turbulence in the open ocean surface boundary layer. *J. Adv. Model. Earth Syst.*, **11**, 4066-4094.
843
844 Buckingham, C. E., J. Gula, and X. Carton, 2020: The role of curvature in modifying frontal
845 instabilities, part 2. *J. Phys. Oceanogr.*, in press.

Busecke, J. J. M., and R. P. Abernathey, 2019: Ocean mesoscale mixing linked to climate variability. *Sci. Adv.*, **5**, eaav5014.

Callies, J., and R. Ferrari, 2013: Interpreting energy and tracer spectra of upper-ocean turbulence in the submesoscale range (1-200 km). *J. Phys. Oceanogr.*, **43**, 2456-2474.

Callies, J., R. Ferrari, J. Klymak, and J. Gula, 2015: Seasonality in submesoscale turbulence. *Nature Comm.*, **6**, 6862.

Callies, J., R. Barkan, and A. C. Naveira Garabato, 2020: Time scales of submesoscale flow inferred from a mooring array. *J. Phys. Oceanogr.*, **50**, 1065-1086.

Callies, J., G. Flierl, R. Ferrari, and B. Fox-Kemper, 2016: The role of mixed-layer instabilities in submesoscale turbulence. *J. Fluid Mech.*, **788**, 5-41.

Cao, H., Z. Jing, B. Fox-Kemper, T. Yan, and Y. Qi, 2019: Scale transition from geostrophic motions to internal waves in the northern South China Sea. *J. Geophys. Res.*, **124**, 9364-9383.

Capet, X., J. C. McWilliams, M. J. Molemaker, and A. F. Shchepetkin, 2008a: Mesoscale to submesoscale transition in the California Current System. Part II: Frontal processes. *J. Phys. Oceanogr.*, **38**, 44-64.

Capet, X., J. C. McWilliams, M. J. Molemaker, and A. F. Shchepetkin, 2008b: Mesoscale to submesoscale transition in the California Current System. Part III: Energy balance and flux. *J. Phys. Oceanogr.*, **38**, 2256-2269.

Chelton, D. B., R. A. deSzoeke, M. G. Schlax, K. El Naggar, and N. Siwertz, 1998: Geographical variability of the first baroclinic Rossby radius of deformation. *J. Phys. Oceanogr.*, **28**, 433-460.

Chelton, D. B., M. G. Schlax, and R. G. Samelson, 2011: Global observations of nonlinear mesoscale eddies. *Prog. Oceanogr.*, **91**, 167-216.

Cusack, J. M., J. A. Brearley, A. C. Naveira Garabato, D. A. Smeed, K. L. Polzin, N. Velzeboer, and C. J. Shakespeare, 2020: Observed eddy-internal wave interactions in the Southern Ocean. *J. Phys. Oceanogr.*, in press.

Damerell, G. M., K. J. Heywood, A. F. Thompson, U. Binetti, and J. Kaiser, 2016: The vertical structure of upper ocean variability at the Porcupine Abyssal Plain during 2012-2013. *J. Geophys. Res.*, **121**, 3075-3089.

D'Asaro, E., C. Lee, L. Rainville, R. Harcourt, and L. Thomas, 2011: Enhanced turbulence and energy dissipation at ocean fronts. *Science*, **332**, 318-322.

de La Lama, M. S., J. H. LaCasce, and H. Fuhr, 2016: The vertical structure of ocean eddies. *Dyn. Stat. Clim. Syst.*, **1**, dzw001.

Dong, J., B. Fox-Kemper, H. Zhang, and C. Dong, 2020: The seasonality of submesoscale energy production, content, and cascade. *Geophys. Res. Lett.*, **47**, e2020GL087388.

Eden, C., and R. J. Greatbatch, 2008: Towards a mesoscale eddy closure. *Ocean Modell.*, **20**, 223-239.

Erickson, Z. K., A. F. Thompson, J. Callies, X. Yu, A. Naveira Garabato, and P. Klein, 2020: The vertical structure of open-ocean submesoscale variability during a full seasonal cycle. *J. Phys. Oceanogr.*, **50**, 145-160.

Eyink, G. L., 2005: Locality of turbulent cascades. *Physica D*, **207**, 91-116.

Ferrari, R., and C. Wunsch, 2009: Ocean circulation kinetic energy: Reservoirs, sources, and sinks. *Ann. Rev. Fluid Mech.*, **41**, 253-282.

Fox-Kemper, B., R. Ferrari, and R. Hallberg, 2008: Parameterization of mixed layer eddies. Part I: Theory and diagnosis. *J. Phys. Oceanogr.*, **38**, 1145-1165.

Frankignoul, C., and K. Hasselmann, 1977: Stochastic climate models, Part II: Application to sea-surface temperature anomalies and thermocline variability. *Tellus*, **29**, 289-305.

Frisch, U., 1995: *Turbulence: The Legacy of A. N. Kolmogorov.*Cambridge University Press, 296 pp.

Gent, P. R., J. Willebrand, T. J. McDougall, and J. C. McWilliams, 1995: Parameterizing eddy-induced tracer transports in ocean circulation models. *J. Phys. Oceanogr.*, **25**, 463-474.

Germano, M., 1992: Turbulence: The filtering approach. *J. Fluid Mech.*, **238**, 325-336.

Gill, A. E., J. S. A. Green, and A. J. Simmons, 1974: Energy partition in the large-scale ocean circulation and the production of mid-ocean eddies. *Deep-Sea Res.*, **21**, 499-528.

Griffies, S. M., 1998: The Gent-McWilliams skew flux. *J. Phys. Oceanogr.*, **28**, 831-841.

Griffies, S. M., M. Winton, W. G. Anderson, R. Benson, T. L. Delworth, C. O. Dufour, J. P. Dunne, P. Goddard, A. K. Morrison, A. Rosati, A. T. Wittenberg, J. Yin, and R. Zhang, 2015: Impacts on ocean heat from transient mesoscale eddies in a hierarchy of climate models. *J. Clim.*, **28**, 952-977.

Haine, T. W. N., and J. Marshall, 1998: Gravitational, symmetric, and baroclinic Instability of the ocean mixed layer. *J. Phys. Oceanogr.*, **28**, 634-658.

Hallberg, R., and A. Gnanadesikan, 2006: The role of eddies in determining the structure and response of the wind-driven Southern Hemisphere overturning: Results from the Modeling Eddies in the Southern Ocean (MESO) project. *J. Phys. Oceanogr.*, **36**, 2232-2252.

Hoskins, B. J., 1982: The mathematical theory of frontogenesis. *Ann. Rev. Fluid Mech.*, **14**, 131-151.

Jing, Z., P. Chang, S. F. DiMarco, and L. Wu, 2018: Observed energy exchange between low-frequency flows and internal waves in the Gulf of Mexico. *J. Phys. Oceanogr.*, **48**, 995-1008.

Klein, P., G. Lapeyre, L. Siegelman, B. Qiu, L.-L. Fu, H. Torres, Z. Su, D. Menemenlis, and S. Le Gentil, 2019: Ocean-scale interactions from space. *Earth Space Sci.*, **6**, 795-817.

Leonard, A., 1974: Energy cascade in large-eddy simulations of turbulent fluid flows. *Adv. Geophys.*, **18**, 237-248.

Llort, J., C. Langlais, R. Matear, S. Moreau, A. Lenton, and P. G. Strutton, 2018: Evaluating Southern Ocean carbon eddy-pump from biogeochemical-Argo floats. *J. Geophys. Res.*, **123**, 971-984.

Marshall, D. P., J. R. Maddison, and P. S. Berloff, 2012: A framework for parameterizing eddy potential vorticity fluxes. *J. Phys. Oceanogr.*, **42**, 539-557.

McDougall, T. J., and P. C. McIntosh, 2001: The temporal-residual-mean velocity. Part II: isopycnal interpretation and the tracer and momentum equations. *J. Phys. Oceanogr.*, **31**, 1222-1246.

McDougall, T. J., and P. M. Barker, 2011: Getting started with TEOS-10 and the Gibbs Seawater (GSW) Oceanographic Toolbox, 28pp., SCOR/IAPSO WG127, ISBN 978-0-646-55621-5.

McWilliams, J. C., 2016: Submesoscale currents in the ocean. *Proc. Roy. Soc. A*, **472**, 20160117.

Menemenlis, D., J.-M. Campin, P. Heimbach, C. Hill, T. Lee, A. Nguyen, M. Schodlok, and H. Zhang, 2008: ECCO2: High resolution global ocean and sea ice data synthesis. *Mercator Quart. News.*, **31**, 13-21.

933 Molemaker, M. J., and J. C. McWilliams, 2010: Local balance and cross-scale flux of available
934 potential energy. *J. Fluid Mech.*, **654**, 295-314.

935 Molemaker, M. J., J. C. McWilliams, and X. Capet, 2010: Balanced and unbalanced routes to
936 dissipation in an equilibrated Eady flow. *J. Fluid Mech.*, **654**, 35-63.

937 Morrow, R., and P. L. Le Traon, 2012: Recent advances in observing mesoscale ocean dynamics
938 with satellite altimetry. *Adv. Space Res.*, **50**, 1062-1076.

939 O'Rourke, A. K., B. K. Arbic, and S. M. Griffies, 2018: Frequency-domain analysis of atmospher-
940 ically forced versus intrinsic ocean surface kinetic energy variability in GFDL's CM2-O model
941 hierarchy. *J. Clim.*, **31**, 1789-1810.

942 Panetta, R. L., 1993: Zonal jets in wide baroclinically unstable regions: Persistence and scale
943 selection. *J. Atmos. Sci.*, **50**, 2073-2106.

944 Poje, A. C., T. M. Özgökmen, D. J. Bogucki, and A. D. Kirwan Jr., 2017: Evidence of a forward
945 energy cascade and Kolmogorov self-similarity in submesoscale ocean surface drifter observations.
946 *Phys. Fluids*, **29**, 020701.

947 Polzin, K. L., 2010: Mesoscale eddy-internal wave coupling. Part II: Energetics and results from
948 PolyMode. *J. Phys. Oceanogr.*, **40**, 789-801.

949 Qiu, B., S. Chen, P. Klein, H. Sasaki, and Y. Sasai, 2014: Seasonal mesoscale and submesoscale
950 eddy variability along the North Pacific Subtropical Countercurrent. *J. Phys. Oceanogr.*, **44**,
951 3079-3098.

952 Rai, S., M. Hecht, M. Maltrud, and H. Aluie, 2021: Scale of oceanic eddy killing by wind from
953 global satellite observations. Science Advances 7, doi:10.1126/sciadv.abf4920.

954 Rhines, P. B., 1975: Waves and turbulence on a beta-plane. *J. Fluid Mech.*, **69**, 417-443.

Rhines, P. B., 1979: Geostrophic turbulence. *Ann. Rev. Fluid Mech.*, **11**, 401-441.

Rieck, J. K., K. Böning, R. J. Greatbatch, and M. Scheinert, 2015: Seasonal variability of eddy kinetic energy in a global high-resolution ocean model. *Geophys. Res. Lett.*, **42**, 9379-9386.

Salmon, R., 1978: Two-layer quasi-geostrophic turbulence in a simple special case. *Geophys. Astrophys. Fluid Dyn.*, **10**, 25-52.

Salmon, R., 1980: Baroclinic instability and geostrophic turbulence. *Geophys. Astrophys. Fluid Dyn.*, **15**, 167-211.

Sasaki, H., P. Klein, B. Qiu, and Y. Sasai, 2014: Impact of oceanic-scale interactions on the seasonal modulation of ocean dynamics by the atmosphere. *Nature Comm.*, **5**, 5636.

Sasaki, H., P. Klein, Y. Sasai, and B. Qiu, 2017: Regionality and seasonality of submesoscale and mesoscale turbulence in the North Pacific Ocean. *Ocean Dyn.*, **67**, 1195-1216.

Scharffenberg, M. G., and D. Stammer, 2010: Seasonal variations of the large-scale geostrophic flow field and eddy kinetic energy inferred from the TOPEX/Poseidon and Jason-1 tandem mission data. *J. Geophys. Res.*, **115**, C02008.

Schubert, R., J. Gula, R. J. Greatbatch, B. Baschek, and A. Biastoch, 2020: The submesoscale kinetic energy cascade: Mesoscale absorption of submesoscale mixed layer eddies and frontal downscale fluxes. *J. Phys. Oceanogr.*, **50**, 2573-2589.

Scott, R. B., and F. Wang, 2005: Direct evidence of an oceanic inverse kinetic energy cascade from satellite altimetry. *J. Phys. Oceanogr.*, **35**, 1650-1666.

Sérazin, G., T. Penduff, B. Barnier, J.-M. Molines, B. K. Arbic, M. Müller, and L. Terray, 2018: Inverse cascades of kinetic energy as a source of intrinsic variability: A global OGCM study. *J. Phys. Oceanogr.*, **48**, 1385-1408.

977 Siegelman, L., 2020: Energetic submesoscale dynamics in the ocean interior. *J. Phys. Oceanogr.*,
978 **50**, 727-749.

979 Smith, K. S., and G. K. Vallis, 2002: The scales and equilibration of midocean eddies:
980 Forced–dissipative flow. *J. Phys. Oceanogr.*, **32**, 1699-1720.

981 Soufflet, Y., P. Marchesiello, F. Lemarié, J. Jouanno, X. Capet, L. Debreu, and R. Benshila, 2016:
982 On effective resolution in ocean models. *Ocean Model.*, **98**, 36-50.

983 Stamper, M. A., and J. R. Taylor, 2016: The transition from symmetric to baroclinic instability in
984 the Eady model. *Ocean Dyn.*, **67**, 65-80.

985 Su, Z., J. Wang, P. Klein, A. F. Thompson, and D. Menemenlis, 2018: Ocean submesoscales as a
986 key component of the global heat budget. *Nature Comm.*, **9**, 775.

987 Sun, B., C. Liu, and F. Wang, 2019: Global meridional eddy heat transport inferred from Argo and
988 altimetry observations. *Sci. Rep.*, **9**, 1345.

989 Taylor, J. R., and R. Ferrari, 2010: Buoyancy and wind-driven convection at mixed layer density
990 fronts. *J. Phys. Oceanogr.*, **40**, 1222–1242.

991 Thomas, L. N., 2005: Destruction of potential vorticity by winds. *J. Phys. Oceanogr.*, **35**,
992 2457-2466.

993 Thomas, L. N., and R. Ferrari, 2008: Friction, frontogenesis, and the stratification of the surface
994 mixed layer. *J. Phys. Oceanogr.*, **38**, 2501-2518.

995 Thompson, A. F., A. Lazar, C. E. Buckingham, A. C. Naveira Garabato, G. M. Damerell, and
996 K. J. Heywood, 2016: Open-ocean submesoscale motions: a full seasonal cycle of mixed layer
997 instabilities from gliders. *J. Phys. Oceanogr.*, **46**, 1285-1307.

998 Tulloch, R., J. Marshall, C. Hill, and K. S. Smith, 2011: Scales, growth rates, and spectral fluxes
999 of baroclinic instability in the ocean. *J. Phys. Oceanogr.*, **41**, 1057-1076.

1000 Uchida, T., R. Abernathey, and S. Smith, 2017: Seasonality of eddy kinetic energy in an eddy-
1001 permitting global climate model. *Ocean Model.*, **118**, 41-58.

1002 Yu, X., A. C. Naveira Garabato, A. P. Martin, D. G. Evans, and Z. Su, 2019a: Wind-forced
1003 symmetric instability at a transient mid-ocean front. *Geophys. Res. Lett.*, **46**, 11281-11291.

1004 Yu, X., A. C. Naveira Garabato, A. P. Martin, C. E. Buckingham, L. Brannigan, and Z. Su, 2019b:
1005 An annual cycle of submesoscale vertical flow and restratification in the upper ocean. *J. Phys.*
1006 *Oceanogr.*, **49**, 1439-1461.

1007 Yu, X., A. C. Naveira Garabato, A. P. Martin, and D. P. Marshall, 2021: The annual cycle of upper-
1008 ocean potential vorticity and its relationship to submesoscale instabilities. *J. Phys. Oceanogr.*, **51**,
1009 385-402.

1010 Zhai, X., 2017: The annual cycle of surface eddy kinetic energy and its influence on eddy
1011 momentum fluxes as inferred from altimeter data. *Sat. Oceanogr. Meteor.*, **2**, 299.

1012 Zhai, X., R. J. Greatbatch, and J.-D. Kohlmann, 2008: On the seasonal variability of eddy kinetic
1013 energy in the Gulf Stream region. *Geophys. Res. Lett.*, **35**, L24609.

LIST OF FIGURES

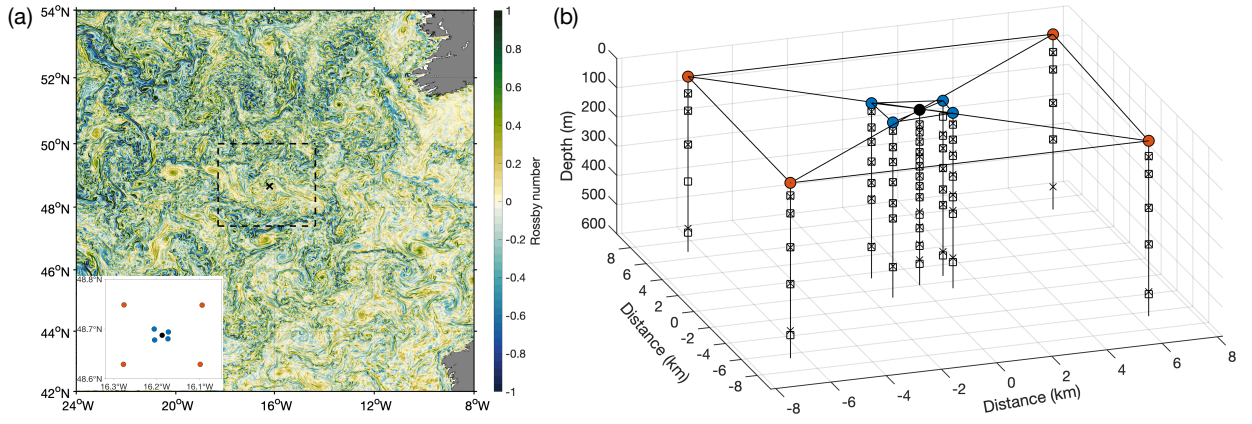

FIG. 1. (a) Map of the study region in the Northeast Atlantic, with Rossby number (quantified as the ratio of relative to planetary vorticities) from a LLC4320 simulation snapshot on 20 December 2011 (shading). The location of the OSMOSIS mooring array is indicated by the cross, and the array's spatial layout is expanded in the inset (central mooring marked by a black circle, inner moorings marked by blue circles, and outer moorings marked by red circles). The dashed rectangle shows the area of the LLC4320 simulation considered in the present analysis. (b) 3-d configuration of the OSMOSIS array, with positions of current meters and CTDs respectively marked by squares and crosses.

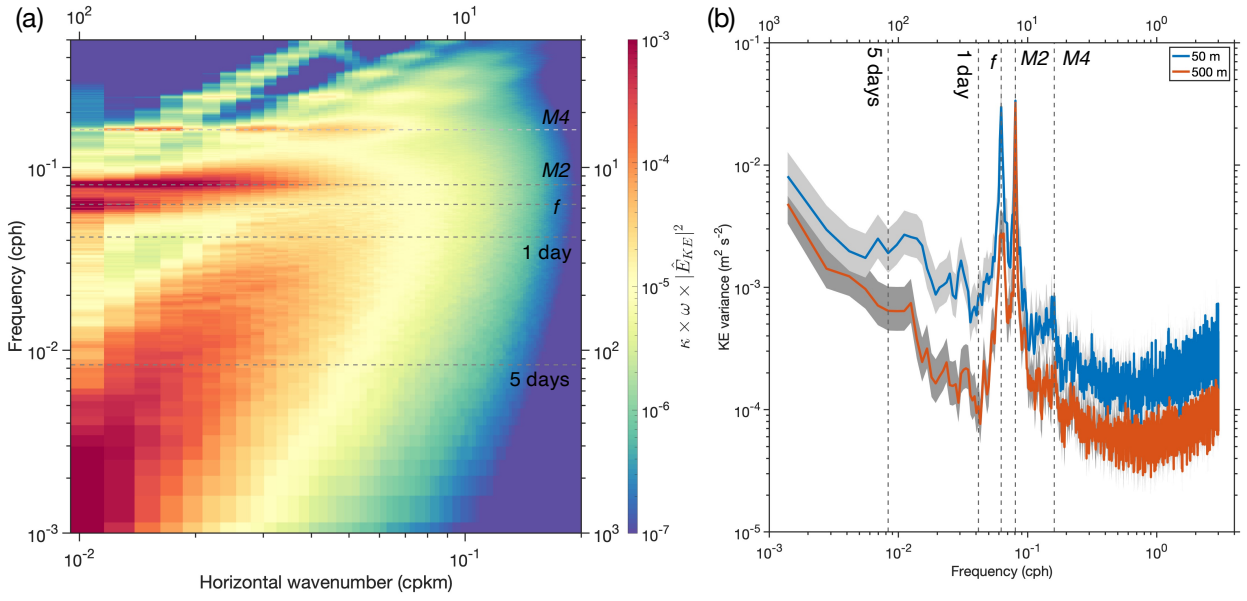

FIG. 2. (a) Frequency - horizontal wavenumber spectrum of KE (multiplied by frequency and horizontal wavenumber) at the surface in the OSMOSIS area in the LLC4320 simulation (dashed rectangle in Figure 1a). (b) Illustrative frequency spectra of KE at 50 m and 500 m in the OSMOSIS mooring observations. Grey shading indicates 95% confidence intervals. Significant periods are marked by dashed lines and labelled in both panels.

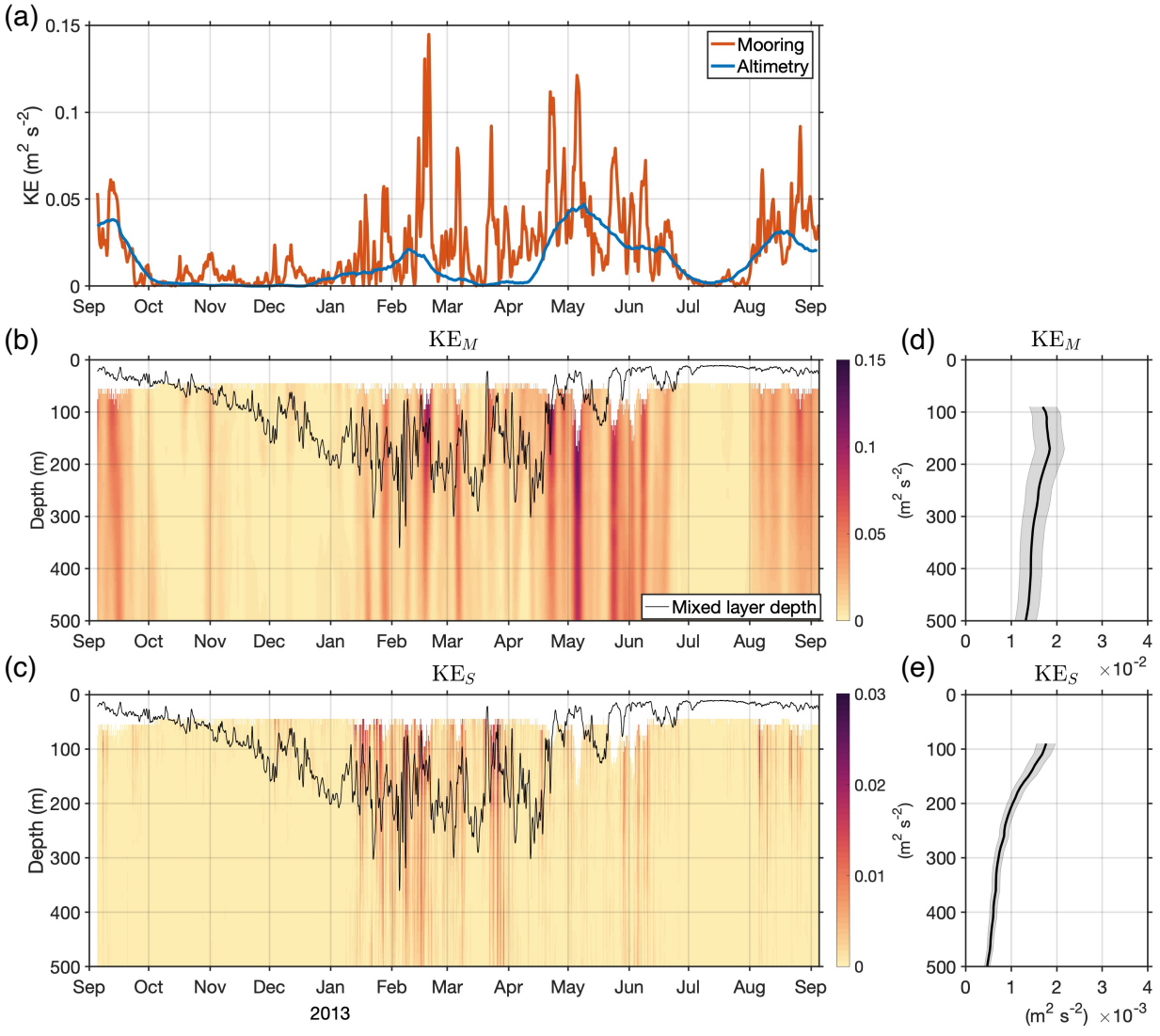

1121 FIG. 3. Time series of (a) KE at a nominal depth of 51 m from the OSMOSIS central mooring observations
1122 (red line), and at the surface from AVISO satellite altimetry (blue line; calculated at the grid point nearest the
1123 central mooring); (b) mesoscale KE; and (c) submesoscale KE. The mixed layer depth as determined from glider
1124 measurements is shown by the black contour in panels (b)-(c). Note the different color bar ranges in panels
1125 (b)-(c). (d) and (e) show the time-mean profiles (black lines) and standard errors (grey shading) of mesoscale
1126 and submesoscale KE, respectively.

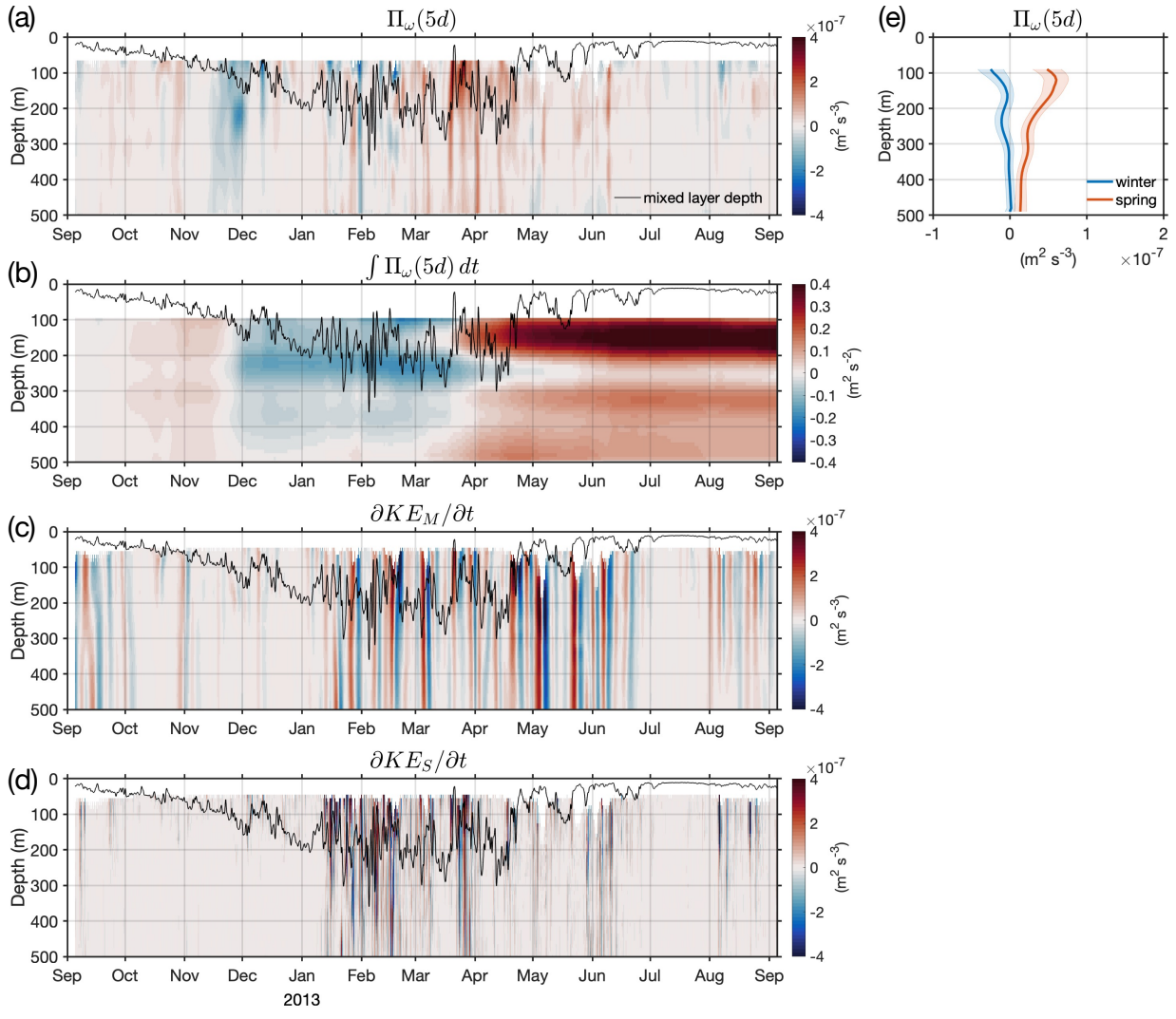

Fig. 4. Time series in the OSMOSIS mooring observations of (a) cross-scale KE transfer between mesoscale and submesoscale motions, Π_ω (with positive values indicating a downscale KE transfer; observational uncertainties in Π_ω are typically $< 4 \times 10^{-8}$ m^2 s^{-3}, see Appendix A); (b) temporal integral of Π_ω; (c) temporal rate of change of mesoscale KE; and (d) temporal rate of change of submesoscale KE. The mixed layer depth as determined from glider measurements is shown by the black contour in panels (a)-(d). The time-mean profiles (solid lines) and standard errors (shading) of cross-scale KE transfers in winter (December to February) and spring (March to May) are shown in (e).

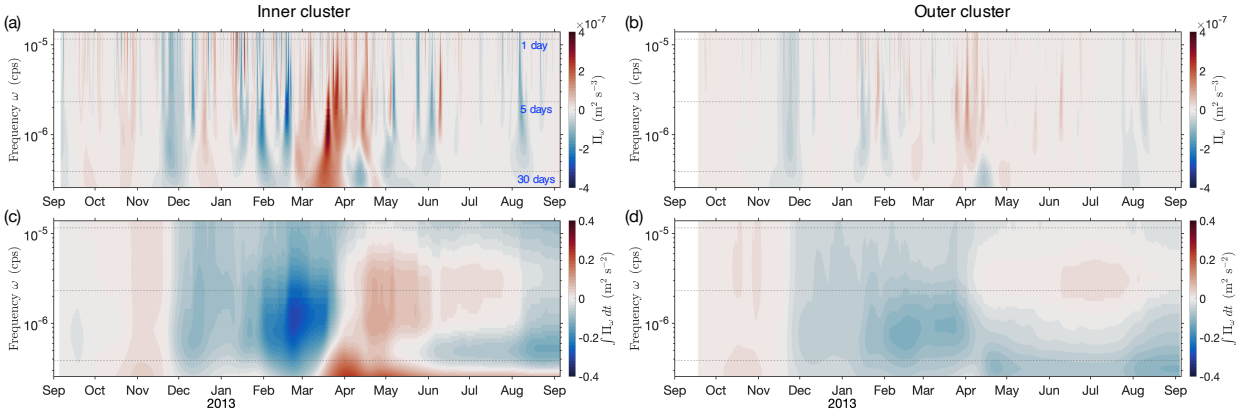

FIG. 5. Time series in the OSMOSIS mooring observations (averaged over the 50 - 150 m depth range) of cross-scale KE transfer, Π_ω (with positive values indicating a downscale KE transfer), as a function of frequency, computed from (a) the central and inner moorings; and (b) the central and outer moorings. The temporal integrals of Π_ω in (a) and (b) are respectively shown in (c) and (d). Significant periods in all panels are marked by dotted lines in all panels, and labelled in (a).

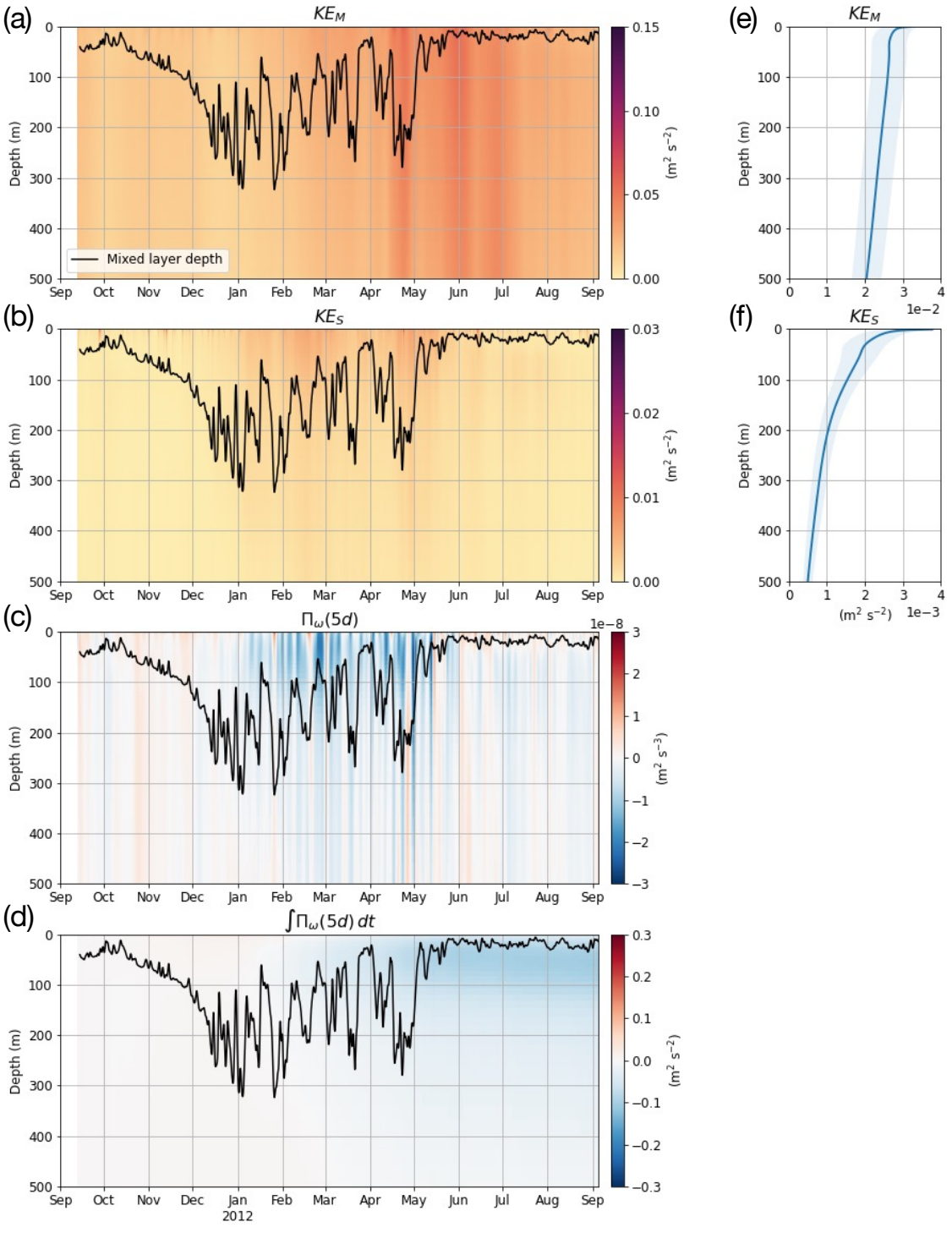

1139 FIG. 6. Time series in the LLC4320 simulation (averages over dashed rectangle in Figure 1a) of (a) mesoscale
1140 KE; (b) submesoscale KE; (c) cross-scale KE transfer between mesoscale and submesoscale motions, Π_ω (with
1141 positive values indicating a downscale KE transfer); and (d) temporal integral of Π_ω. The mixed layer depth is
1142 shown by the black contour in panels (a)-(d). d) and (e) show the time-mean profiles (solid lines) and standard
1143 errors (shading) of mesoscale and submesoscale KE, respectively.

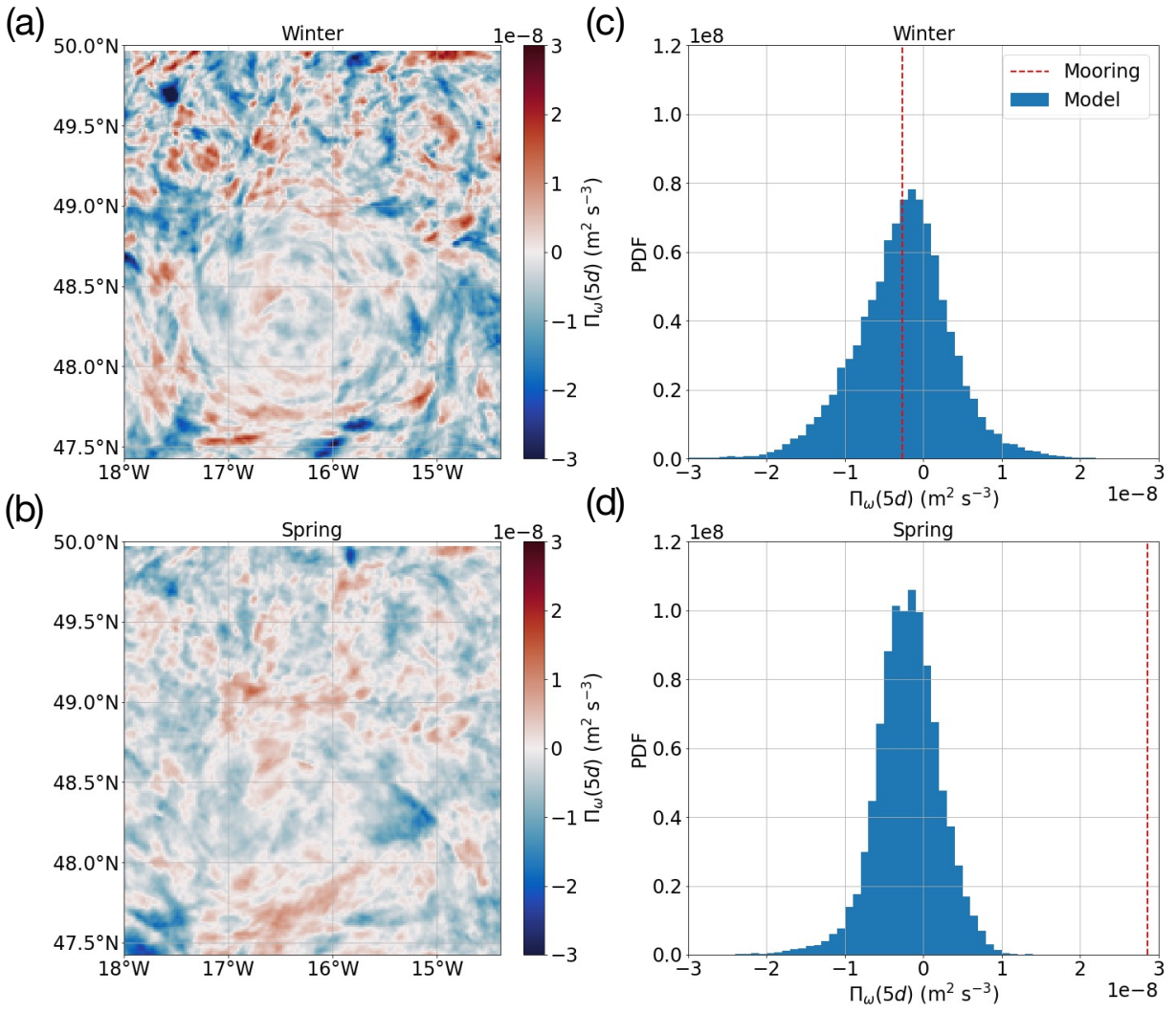

1144 FIG. 7. Time-mean and depth-averaged (over the 50-520 m range) cross-scale KE transfer between mesoscale
1145 and submesoscale motions, Π_ω (with positive values indicating a downscale KE transfer), in (a) winter (December
1146 to February) and (b) spring (March to May), for the LLC4320 simulation. Panels (c) and (d) respectively show
1147 probability distribution functions of Π_ω for the simulation in winter and spring. The dashed red lines in (c)-(d)
1148 indicate the seasonal-mean values of Π_ω diagnosed from the OSMOSIS moorings.

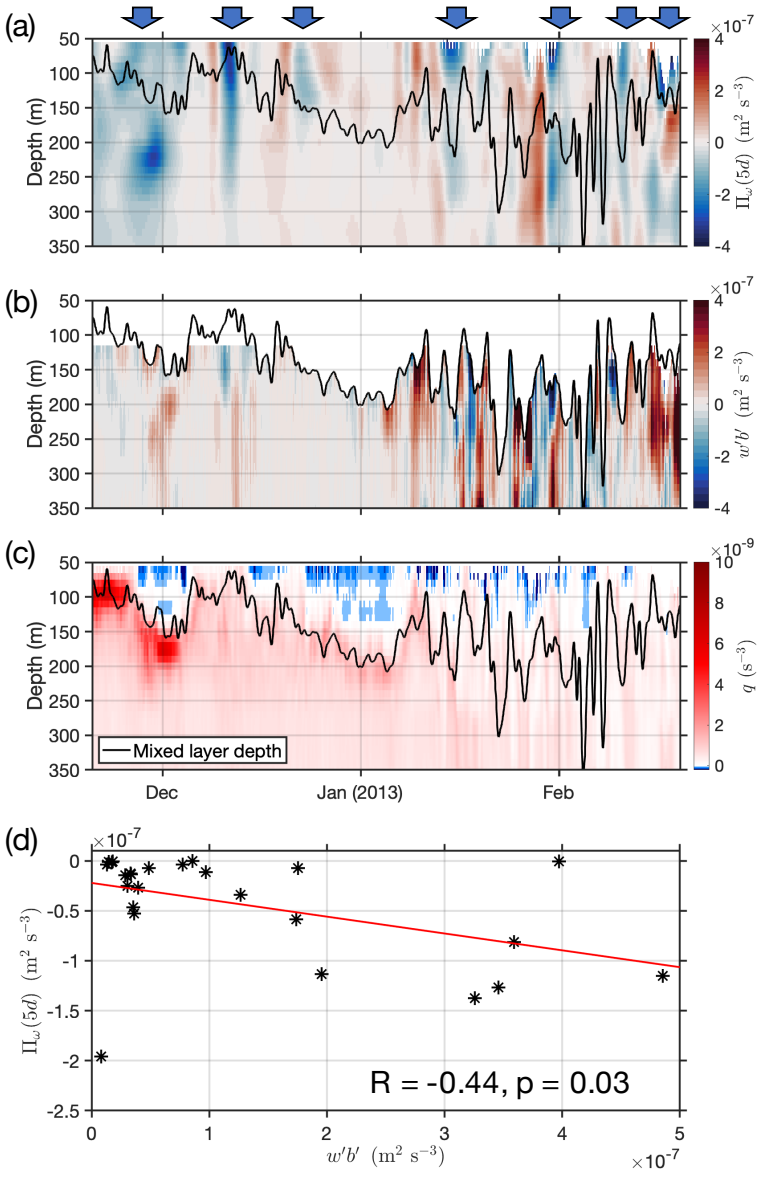

FIG. 8. Winter time series in the OSMOSIS mooring observations of (a) cross-scale KE transfer between mesoscale and submesoscale motions, Π_ω (with positive values indicating a downscale KE transfer); (b) vertical buoyancy flux, $w'b'$; and (c) potential vorticity, q, negative values of which indicate propensity to the development of submesoscale (gravitational and symmetric) instabilities. Blue arrows on the upper axis of (a) indicate the main events of upscale KE transfer. The mixed layer depth as determined from glider measurements is shown by the black contour panels (a)-(c). (d) Scatter diagram of the relationship between the vertical buoyancy flux for instances of positive (i.e. re-stratifying) $w'b'$ and Π_ω. The coefficient of correlation (R) between the two variables and associated p-value are indicated.

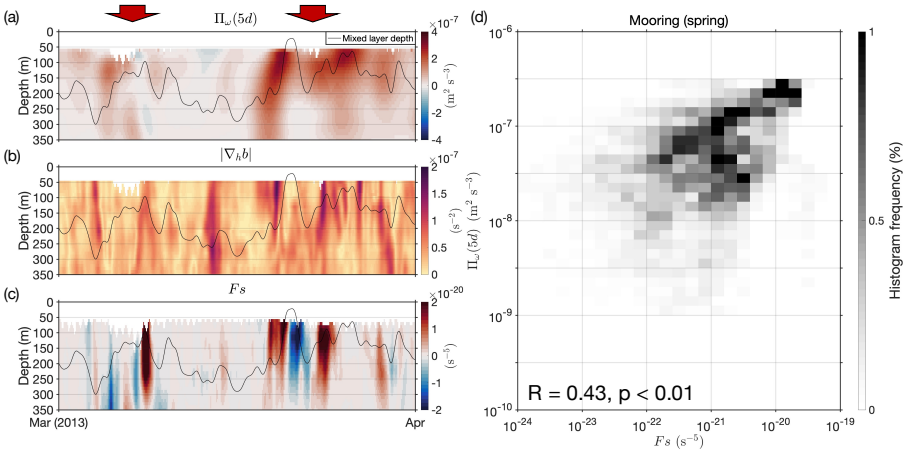

FIG. 9. Spring time series in the OSMOSIS mooring observations of (a) cross-scale KE transfer between mesoscale and submesoscale motions, Π_ω (with positive values indicating a downscale KE transfer); (b) submesoscale lateral buoyancy gradient magnitude, $|\nabla b|$; and (c) mesoscale frontogenesis function, F_S (with positive and negative values respectively indicating frontogenesis and frontolysis). Red arrows on the upper axis of (a) indicate the main events of downscale KE transfer. The mixed layer depth as determined from glider measurements is shown by the black contour panels (a)-(c). (d) Histogram synthesis of the relationship between positive F_S and Π_ω for all depth levels between 50 m and 520 m. The coefficient of correlation (R) between the two variables and associated p-value are indicated.

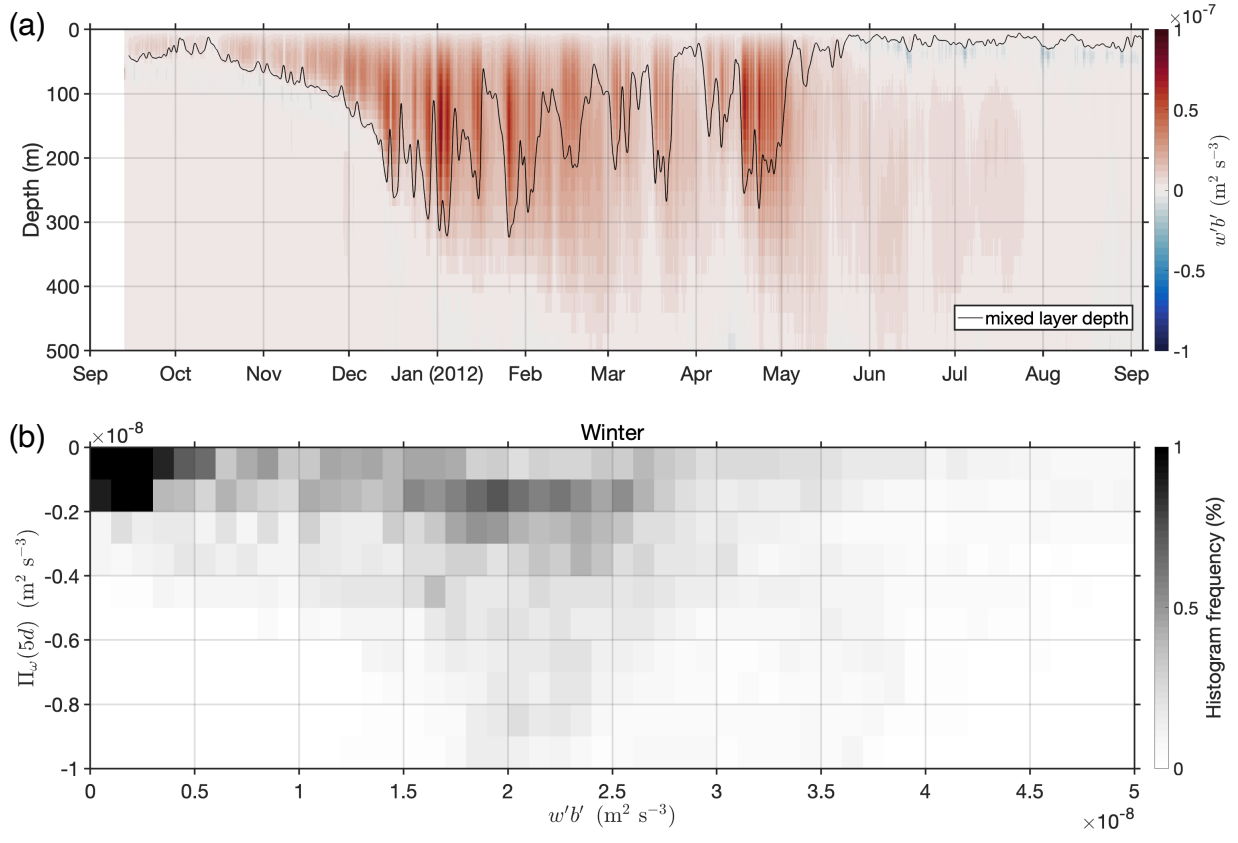

FIG. 10. (a) Time series of the spatially-averaged vertical buoyancy flux, $w'b'$, in the LLC4320 simulation. The spatially-averaged mixed layer depth is shown by the black contour. (b) Histogram depiction of the relationship between Π_ω and the vertical buoyancy flux for instances of positive (i.e. re-stratifying) $w'b'$ in winter (December to February). Values of both variables are averages over the 50-520 m depth range.

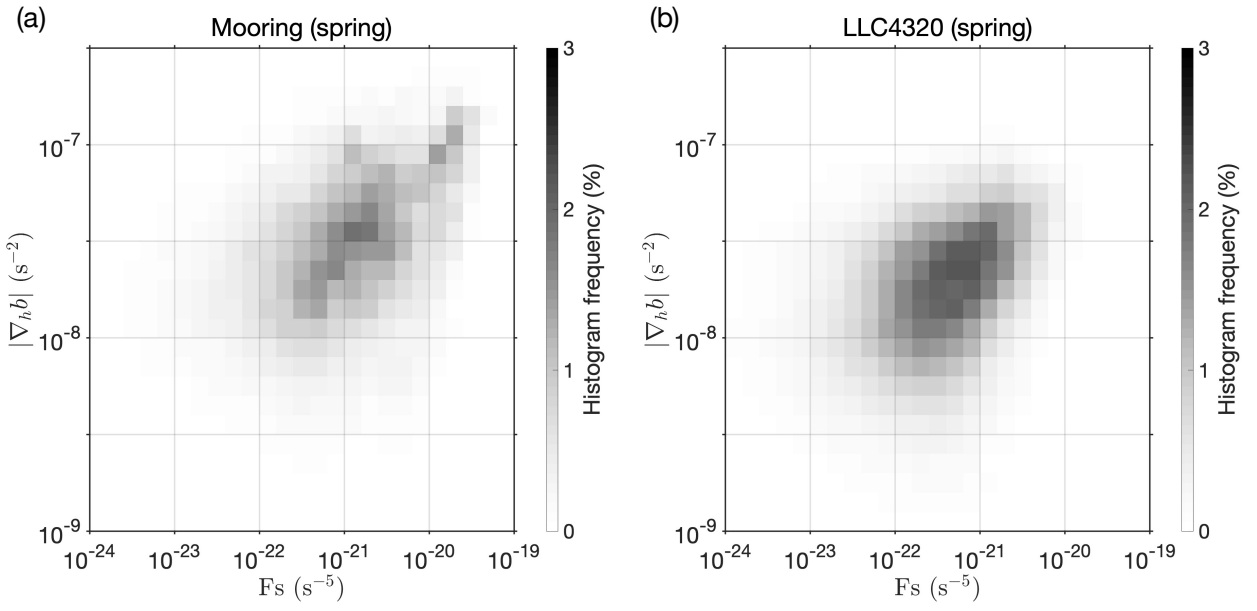

1169 FIG. 11. Histogram depictions of the relationship between positive values of the mesoscale frontogenesis
1170 function, F_S, and the submesoscale lateral buoyancy gradient magnitude, $|\nabla b|$, in spring (March to May), in (a)
1171 the OSMOSIS mooring observations, and (b) the LLC4320 simulation. Values of all variables are averages over
1172 the 50-520 m depth range.

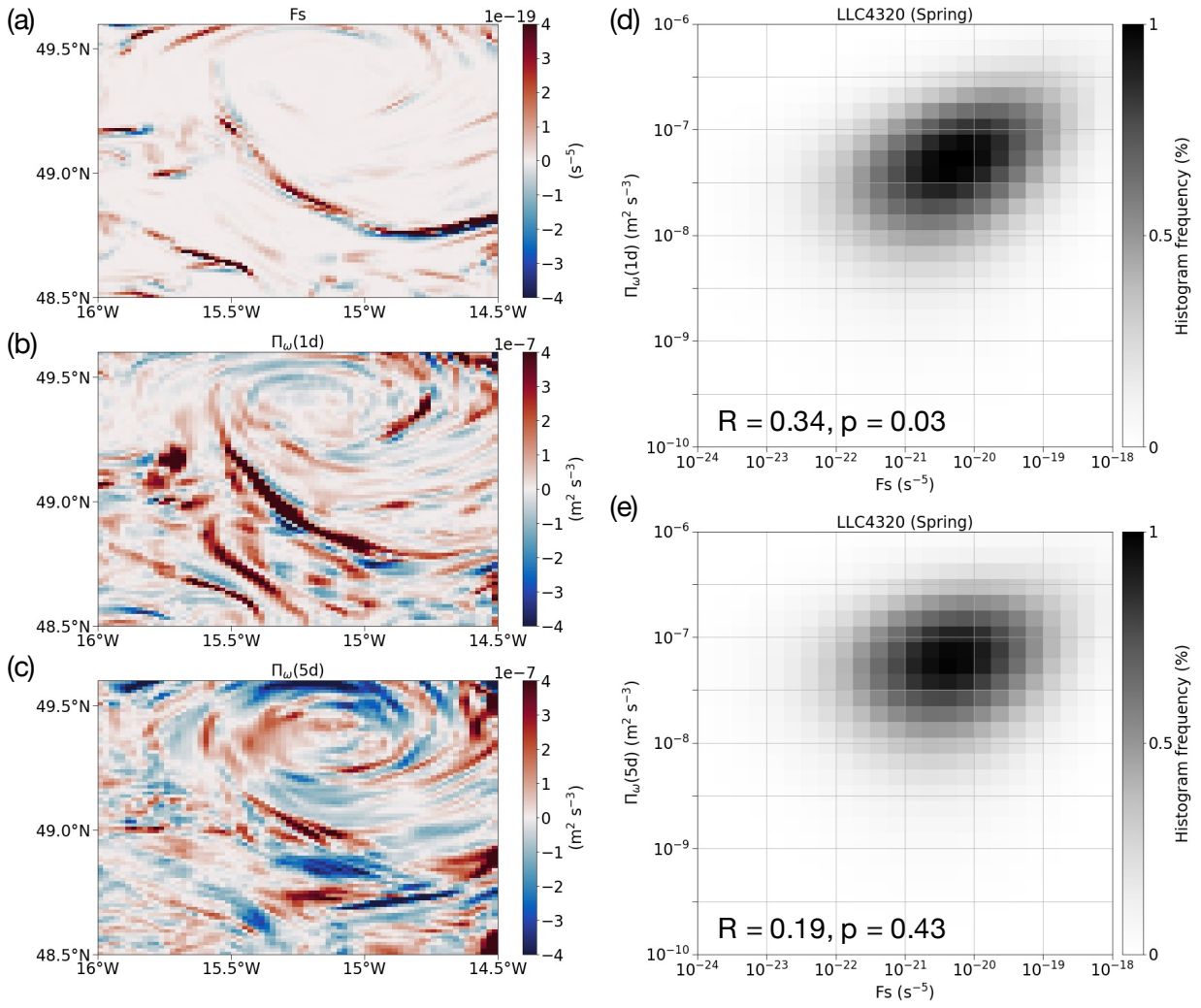

FIG. 12. Surface snapshots of (a) mesoscale frontogenesis function F_S, (b) cross-scale KE transfer at a period of 1 day, and (c) cross-scale KE transfer at a period of 5 days, on 7 March 2012 in the LLC4320 simulation. Histogram depictions of the springtime (March to May) relationship between positive values of the mesoscale frontogenesis function and the cross-scale KE transfer at a period of either (d) 1 day or (e) 5 days at the surface are also shown.

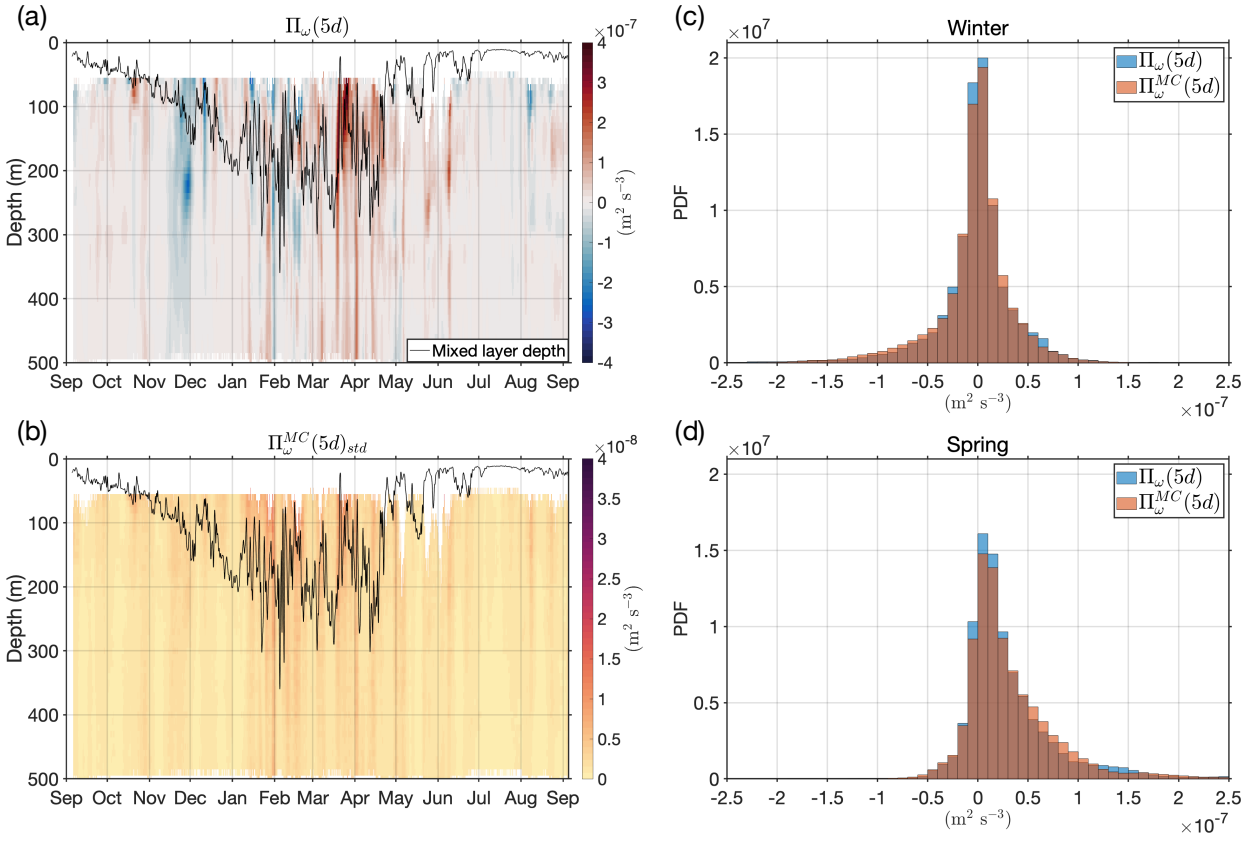

Fig. A1. Time series of (a) cross-scale KE transfer between mesoscale and submesoscale motions diagnosed from the OSMOSIS mooring observations, Π_ω (with positive values indicating a downscale KE transfer); and (b) standard deviation of Π_ω in the 1000 Monte Carlo simulations of mooring motion and instrumental errors (Appendix A). Probability distribution functions of depth-averaged Π_ω diagnosed from the observations (in blue) and the 1000 Monte Carlo simulations of mooring motion and instrumental errors (in red) in (c) winter (December to February) and (d) spring (March to May).

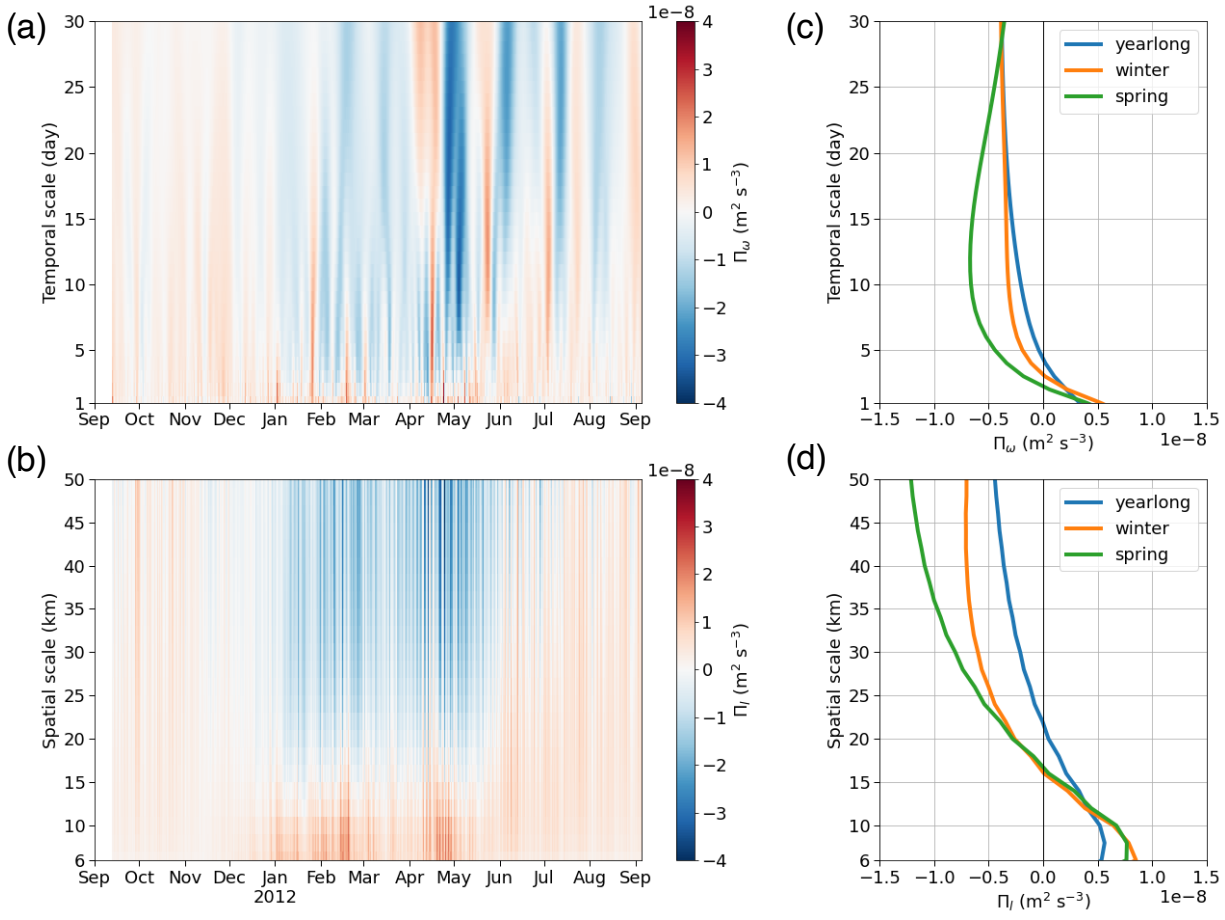

Fig. A2. Time series of the cross-scale KE transfer at the surface in the LLC4320 simulation computed as a function of (a) time scale, and (b) horizontal scale. Mean cross-scale KE transfers for the entire year, winter (December to February) and spring (March to May) are also shown as a function of (c) time scale, and (d) horizontal scale.

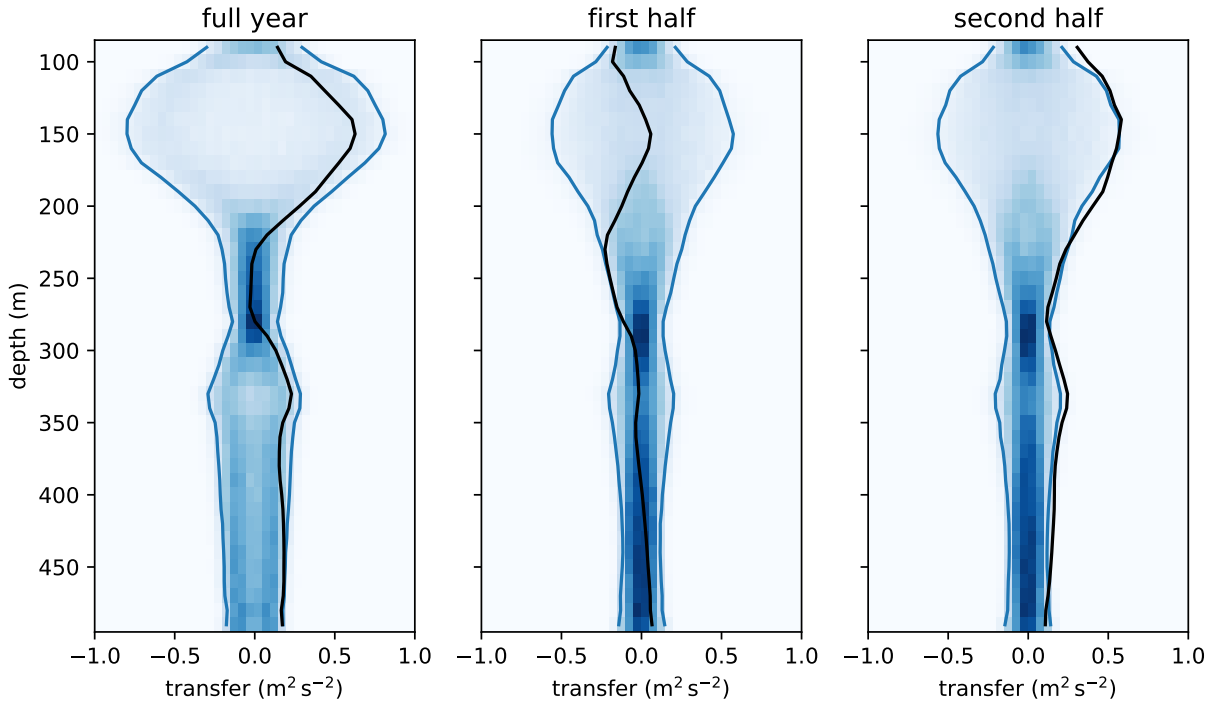

Fig. A3. Statistical significance analysis for the KE transfer between mesoscale and submesoscale motions, Π_ω (with positive values indicating a downscale KE transfer). The shading shows estimates of the probability density functions for a zero-transfer flow with the same amplitude as observed. The blue lines show the upper and lower boundaries of the 95% confidence intervals, and the black lines the observed transfer values. The diagnostics are shown for the cumulative transfer over the full year, as well as split into the first and second halves of the year.